



A ductility criterion for bcc high entropy alloys

Eleanor Mak^{*}, Binglun Yin, W.A. Curtin

Laboratory for Multiscale Mechanics Modeling, Institute of Mechanical Engineering, École polytechnique fédérale de Lausanne (EPFL), Lausanne CH-1015, Switzerland

ARTICLE INFO

Keywords:

Fracture

Bcc

High entropy alloys

Intrinsic ductility

ABSTRACT

A current goal driving alloy development is the identification of alloy compositions for high temperature applications but with the additional requirement of sufficient ductility at ambient temperatures. Multicomponent, single-phase, polycrystalline High Entropy Alloys (HEAs) have recently emerged as a new class of metal alloys, and some refractory bcc HEAs composed mainly of Nb, V, Ta, Cr, Mo, and/or W show excellent strength retention up to very high temperatures but low ductility at room temperature (RT). Here, it is postulated that the macroscopic ductility in bcc elements and alloys is determined by the intrinsic competition between brittle cleavage and ductile dislocation emission mechanisms at an atomistically sharp crack. The stress intensities K_{Ic} for cleavage and K_{Ie} for emission are evaluated within Linear Elastic Fracture Mechanics and validated by atomistic simulations on model alloys. A RT ductility criterion based on K_{Ie}/K_{Ic} for critical crack orientations is proposed based on the elemental metals and is then applied to HEAs. Agreement with experimental trends in ductility vs. composition across a range of existing HEAs is demonstrated. The analysis is then extended across large composition spaces of the Mo-Nb-Ta-V-W and Mo-Nb-Ti alloy families, identifying new compositions with the potential for RT ductility.

1. Introduction

The demand for metal alloys with superior structural and functional performance in industrial applications continues to increase, especially as the need for more-energy-efficient components becomes important. Recently, a new class of metal alloys has emerged, the High Entropy Alloys (HEAs) (Miracle et al., 2014; Miracle and Senkov, 2017; Gorsse et al., 2017), which consist of many elemental components all at non-dilute concentrations and forming a single-phase polycrystalline material. Most HEAs studied to date are near-equiatomic and forming in fcc, bcc, or hcp crystal structures. One major classes of HEAs are the fcc late transition metal alloys in the Co-Cr-Fe-Mn-Ni-Cu family, with the original CoCrFeMnNi Cantor alloy being the most widely studied. Another major class of HEAs are the bcc refractory metal alloys in the Cr-Mo-Nb-Ta-V-W-Hf-Ti-Zr family. These bcc HEAs have high yield stresses at room temperature and some also have excellent strength retention up to high temperatures (1000 C or more) (Senkov et al., 2010, 2011b,a, 2012, 2014, 2018), making them attractive for high temperature applications. However, many of the alloys with impressive high temperature strength have low ductility at room temperature, limiting their formability and applications. While new theoretical advances are providing a quantitative understanding of the yield stress versus composition and temperature in these bcc HEAs (Maresca and Curtin, 2020a,b; Rao et al., 2019b), there is no understanding of the ductility of these alloys. The identification of novel alloy compositions with both high ductility at ambient temperatures and high strength at high temperatures is a goal that is driving current alloy development.

^{*} Corresponding author.

E-mail address: eleanor.mak@epfl.ch (E. Mak).

The bcc HEAs can have low ductility even in compression, suggesting that the failure is connected to fracture phenomena rather than traditional ductile failure mechanisms and necking failure according to the macroscopic Considère criterion. The refractory bcc elements (Nb, V, Ta, Cr, Mo, W) also exhibit a relatively sharp brittle-to-ductile transition with increasing temperature, being quite brittle (low failure strain and low fracture toughness) at very low temperatures. Thus, the issue of ductility in bcc metals goes beyond the new class of HEAs. The brittle-to-ductile transition in the bcc elements has been attributed to rate-dependent plasticity effects and the shielding of a crack by surrounding dislocations (Hirsch and Roberts, 1991; Gumbsch, 2003). However, the brittle-to-ductile transition is quite abrupt whereas dislocation plasticity shows a smooth dependence on temperature and strain rate. In addition, there is no clear correlation between RT yield strengths and ductility. For instance, in W-Re the Ductile–Brittle Transition Temperature (BDTT) decreases steadily with increasing Re content, with a small amount of tensile ductility at RT achieved at 25% Re, but the yield strength at 7% and 25% Re is comparable to or higher than pure W (Raffo, 1969). In the HEAs, MoNbTaW has very low ductility with a yield strength below 1 GPa (Senkov et al., 2011b) whereas MoNbTaTi has a yield strength above 1.2 GPa yet compression ductility of $\approx 25\%$ (Courty et al., 2019). Examining stress levels beyond yield, the MoNbTaVW alloy supports a maximum stress of about 1.25 GPa at RT but has very low ductility (Senkov et al., 2011b) while NbTaTiW supports a stress of nearly 1.8 GPa at 20% strain (Courty et al., 2019). It thus remains useful to pursue additional new lines of study to connect ductility to alloy composition.

Nearly all experimental studies of ductility of these bcc HEAs so far have been conducted in compression, in part due to the large sample sizes required for tensile testing, but also driven by an industrial interest in formability. We use compressive failure strains as a surrogate measure of the macroscopic ductility in the absence of available tensile data. There is some experimental evidence from very brittle HEAs (e.g. Senkov et al., 2011b) that the primary failure mode in compression is tensile rather than shear. The ductility in moderately ductile HEAs tends to be slip-dominated (e.g. Senkov et al., 2019) and the eventual compression failure by fracture is generally an outcome of the interaction between the localization of the deformation, as expressed by macroscopic shear bands, and grain boundaries. The observed compressive ductility is thus related to an intrinsic resistance to tensile failure.

Here, we postulate that the ductility of bcc elements and alloys is controlled by the intrinsic fracture behavior at a sharp crack tip in the material. The intrinsic fracture behavior of a material is dictated by the competition between dislocation emission and brittle cleavage at an atomistically sharp crack tip. A material is intrinsically ductile if dislocation emission, occurring at a crack-tip mode I stress intensity factor K_{Ie} , occurs prior to cleavage fracture, occurring at a crack-tip mode I stress intensity factor K_{Ic} . Dislocation emission blunts the sharp crack tip and is the enabling mechanism for the subsequent onset of ductile failure mechanisms (void nucleation, growth, and coalescence ahead of the crack). Otherwise, a sharp crack remains sharp and propagates easily. Even if the crack remains sharp, the material can be deforming due to dislocation plasticity in the plastic zone around the crack tip, and this provides additional energy dissipation. The macroscopic toughness is thus higher than the Griffith cleavage value but remains far lower than the toughness achievable by ductile failure mechanisms. Thus, the transition between high toughness (ductile mechanisms) and low toughness (cleavage plus surrounding plasticity) can be a sharp transition ultimately connected to the nanoscale crack tip behavior (cleavage or dislocation emission). Supporting this analysis approach, Ohr (Ohr, 1985) reviewed TEM studies of crack tip deformation in Nb, Mo, and W at room temperature and reported extensive emission and blunting in Nb, moderate emission with cracking in Mo, and some emission with extensive cracking in W. While these experiments were not performed in pure mode I loading, with mixed mode loading argued to facilitate emission, the trend across these elements is consistent with the observed BDTT.

Based on the above postulate, we examine the intrinsic fracture behavior of refractory bcc elements and HEAs within the framework of Linear Elastic Fracture Mechanics (LEFM). The applicability of LEFM is first evaluated quantitatively using atomistic simulations on model HEAs alloys, putting the LEFM analysis on a firm quantitative foundation for bcc metals. We examine full dislocation emission only, neglecting twinning because it is not observed experimentally (Ohr, 1985) and because the generalized fault surfaces for the metals studied here show no stable stacking faults that would enable twinning mechanisms. Through correlation of the intrinsic fracture behavior and the macroscopic ductility of elemental Mo, Nb, Ta, V, and W, we then establish a criterion for room temperature ductility in bcc metals and alloys. The LEFM theory is then applied to HEAs. The relevant material properties (elastic constants, surface energies, unstable stacking fault energies) are obtained from first-principles and appropriately scaled interatomic potentials. Predictions are then made for many single-phase alloys in the Cr-Mo-Nb-Ta-Ti-V-W family that have been studied experimentally, and results agree well with experimental trends. Finally, we extend the analysis across a large composition range in the Mo-Nb-Ta-V-W and Mo-Nb-Ti families to identify promising alloys for future investigation.

Recently, Li et al. (2020) has performed a very similar LEFM-based analysis on five selected HEAs using a different (less-accurate but more-efficient) first-principles method. They computed the ratio of emission to cleavage stress intensities and reported a trend of increasing K_{Ie}/K_{Ic} versus alloy Valence Electron Count (VEC). The alloys with lower K_{Ie}/K_{Ic} are experimentally ductile and those with higher K_{Ie}/K_{Ic} are experimentally brittle (low ductility). However, Li et al. did not examine the bcc elements, did not make a detailed comparison with experiments, did not execute a broader study across the composition space, nor did they validate the use of LEFM; all of these aspects are features of the current work that are complementary to the study of Li et al.. Very new work by Hu et al. (2021) also adopted the same general framework and computed the ratio (surface energy)/(unstable stacking fault energy) that is a major factor in determining K_{Ie}/K_{Ic} . They analyzed one crack orientation (denoted 110/110 below) and developed a very nice reduced order model trained on extensive (but less-stringent) first-principles Density Functional Theory (DFT) computations of the relevant energies. They showed a correlation of the energy ratio with compressive failure strain across a number of HEAs and examined a broad composition space. However, Hu et al. did not validate the LEFM, did not directly address the quantity K_{Ie}/K_{Ic} that involves additional elasticity factors, and did not study multiple crack orientations. The current work is thus complementary to the work of Hu et al. in these respects.

The remainder of this paper is arranged as follows. In Section 2, we briefly review the intrinsic competition between cleavage and dislocation emission crack tip mechanisms within the context of LEFM and then validate the LEFM theory using atomistic simulations. We apply the LEFM theory to predict intrinsic ductility and assess these predictions against trends in experimental ductility, first for several refractory bcc elements in Section 3 and then for many HEAs in Section 4. In Section 5, we extend the analysis to predict ductility over a broad array of HEAs compositions.

2. Intrinsic ductility in bcc crystals: cleavage vs dislocation emission

2.1. Theory

The LEFM solutions for sharp cracks in anisotropic media for plane-strain, infinitesimal deformation are well-established in the literature (e.g. [Ting, 1996](#)). The competition between brittle cleavage and ductile dislocation emission mechanisms are evaluated in terms of the crack-tip mode I stress intensity K_I . The critical stress intensity for cleavage K_{Ic} is given by the Griffith condition, ([Griffith and Taylor, 1921](#))

$$K_{Ic} = \sqrt{\frac{2\gamma_s}{\Lambda_{22}}} \quad (1)$$

where γ_s is the surface energy of the crack plane and Λ_{22} is an anisotropic elasticity parameter defined in the Stroh formalism ([Ting, 1996](#)). Cleavage is thermodynamically precluded at loads below K_{Ic} but can be there can be a lattice-trapping barrier at K_{Ic} , as shown in simulations below.

The critical stress intensity for emission K_{Ie} is well-estimated using the Rice model ([Rice, 1992](#)),

$$K_{Ie} = \sqrt{G_{Ie} o(\phi, \theta) / F_{12}(\theta) \cos(\phi)} \quad (2)$$

where the critical energy release rate for dislocation emission $G_{Ie} = \gamma_{usf}$ is equal to the unstable stacking fault (USF) energy of the emission plane, $F_{12}(\theta)$ is a geometric parameter, and $o(\phi, \theta)$ is another anisotropic elastic parameter. An improved criterion for G_{Ie} that includes the energy cost of creating additional surface due to the step or ledge created by slip was developed by [Andric and Curtin \(2017\)](#). That theory reduces to the Rice relationship when $\gamma_s^e < 3.45\gamma_{usf}$, where γ_s^e is the surface energy of the emission plane. This condition is satisfied by all the materials studied here and so the Rice condition is used here. [Andric et al. \(2019\)](#) later analyzed so-called tension–shear coupling, wherein the USF is proposed to be reduced by the high tension at the crack tip, facilitating emission. They showed that there is no tension dependence to the USF in several fcc and hcp metals, and that there is no effect of tension stresses on emission in ideal mode II loading where the Rice criterion is directly applicable, so that the original Rice condition remains valid. While the dependence of the USF on tension in bcc metals has not been studied to date, there is no a priori basis for assuming such an effect and so tension/shear coupling is neglected here. Finally, we reiterate that twinning is not considered since it is not observed nor expected based on the generalized stacking fault energy surfaces of metals studied here.

The intrinsic ductility criterion is then the ratio of the emission and cleavage stress intensities, and a material is *intrinsically* ductile if the ductility index D satisfies

$$D = \frac{K_{Ie}}{K_{Ic}} = \chi \tilde{\gamma} < 1 \quad (3)$$

where the two quantities

$$\begin{aligned} \chi &= \frac{\sqrt{\Lambda_{22} o(\phi, \theta)}}{\sqrt{2 \cos(\phi) F_{12}(\theta)}} \\ \tilde{\gamma} &= \sqrt{\frac{\gamma_{usf}}{\gamma_s}} \end{aligned} \quad (4)$$

separate the material energetic effects and the anisotropic elastic effects. The LEFM analysis thus requires only a few material parameters: elastic moduli C_{ij} , surface energy of the cleavage planes γ_s , unstable stacking fault energy of the emission planes γ_{usf} , and the fracture geometry. For bcc crystals, it is the $\{100\}$ and $\{110\}$ planes that are typically favored for cleavage ([Tyson et al., 1973](#)). The crack orientations on these planes that most-favor mode I nucleation of edge dislocations are shown in [Fig. 1](#). Since growth of a crack requires crack extension in all in-plane directions, the crack must encounter these most-favorable orientations for emission, and so it is these orientations for which the intrinsic ductility analysis must be applied.

For clarity in later discussion, we will refer to crack orientations in terms of the cleavage and emission plane, e.g. orientation 110/112 refers to a crack on the $\{110\}$ (cleavage) plane and emission on the $\{112\}$ plane corresponding to a $(110)[\bar{1}\bar{1}0]$ crack front (see [Fig. 1](#)). The χ parameter is independent of the absolute value of the elastic constants, and only depends on the elastic anisotropy. For reference, [Fig. 1](#) shows the isotropic value of χ for each orientation; note that the value for 110/112 is much lower than that for 110/110, making it intrinsically more favorable for emission. As we shall see, the 100/110 and 110/112 are the controlling orientations for ductile behavior in their respective crack planes. The degree of elastic anisotropy varies across the bcc materials considered here. For the 110/112 orientation, the effects of elastic anisotropy are weak so that $\chi/\chi_{iso} \sim 1$; the trends in intrinsic fracture behavior are then dominated by the surface and unstable stacking fault energies contained in $\tilde{\gamma}$. In contrast, for the 100/110 orientation, the effects of elastic anisotropy can increase χ up to $\chi/\chi_{iso} \sim 1.1$, which decreases the ductility relative to the isotropic limit. In general we consider full anisotropy in all results presented here.

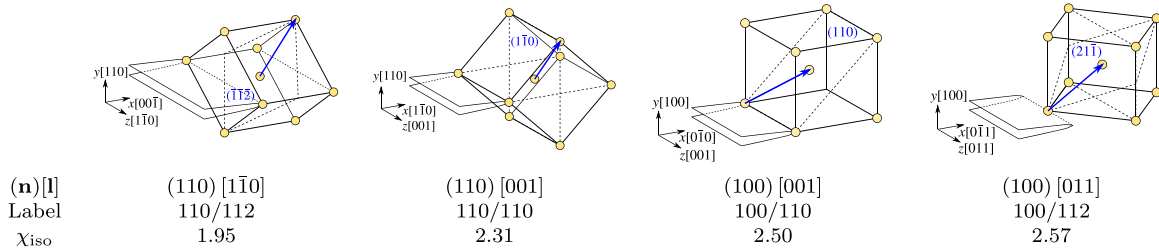


Fig. 1. Geometry of crack orientations (n)[l] favoring $a/2\langle 111 \rangle$ edge dislocation nucleation in mode I fracture. (n) is the crack plane and [l] is the orientation of the crack front. For convenience, we label these orientations in terms of the cleavage and emission plane as indicated. For each orientation, the value of the elasticity parameter for an isotropic material χ_{iso} ($\nu = 0.33$) is also shown. Analysis reveals that the two orientations controlling ductility on the two cleavage planes are the 110/112 and 100/110 orientations.

2.2. Validation of LEFM using atomistic simulations

The LEFM Griffith theory for the cleavage K_{Ic} is based on an exact thermodynamic statement. The LEFM prediction for the emission K_{Ie} is, however, an estimate and so it is important to validate that prediction as best as possible. The theory for K_{Ie} has been compared very carefully to simulations of emission in fcc and hcp metals described by EAM potentials, and has been shown to be generally good (Andric and Curtin, 2017; Mak and Curtin, 2020). These validation studies are encouraging but the accuracy of the theory as applied to bcc crystals should nonetheless be demonstrated. Furthermore, both cleavage (above K_{Ic}) and emission are thermally-activated events. Lattice trapping creates a finite energy barrier for cleavage at the Griffith K_{Ic} . Thermal activation is then relevant above K_{Ic} , which is a lower bound since ideal brittle fracture is governed by thermodynamics. Conversely, emission can occur at lower K_I with some energy barrier due to thermal activation, so K_{Ie} is an upper bound. The operative thermally-activated cleavage and emission stress intensities can thus be closer than the values of K_{Ie} and K_{Ic} computed at $T = 0$ K in LEFM. We remark that the values of both K_{Ic} and K_{Ie} are expected to decrease with increasing temperature since elastic constants, surface, and fault energies are all temperature dependent. The ratio between K_{Ie} and K_{Ic} is thus expected to be minimally dependent on temperature, especially at RT for the high-melting-point refractory alloys of interest here.

Here we validate the theory using a set of EAM-type interatomic potentials by Zhou et al. (2001). These potentials are not quantitative for real materials but have well-defined alloy properties and so serve well as a set of model alloys. For each HEA, we use the average-atom potential (Varvenne et al., 2016) constructed from the elemental Zhou et al. potentials because we wish to validate LEFM, which involves only the average material properties. So, we do not consider the actual random atomistic environments along the crack front that exist in the real random alloy, which is beyond the scope of LEFM.

The standard atomistic simulation method for testing fracture theories is the “K-test” framework (Andric and Curtin, 2019). Unfortunately, direct K-test simulations of atomistic fracture commonly display unphysical behavior at the sharp crack tip. This is due to problems within the interatomic potentials despite producing reasonable and artifact-free material properties (elasticity, surface energy, USF energy) that control the crack tip phenomena of interest. This is particularly true for bcc crystals, with bcc Fe well-studied in particular (Möller and Bitzek, 2014) and our own studies showing similar problems for the Zhou et al. family of potentials for both the bcc elements and their random alloys. For example, a sharp crack will commonly undergo accumulated structural distortions, not unlike amorphization, rather than cleavage; any fracture behavior is then essentially fictitious. More generally, there is also no way to validate K_{Ie} in (intrinsically) brittle materials using direct K-test simulations because a crack will simply grow by cleavage at $K_{Ic} < K_{Ie}$ before reaching the higher value of K_{Ie} . To overcome these difficulties, we use the Nudged-Elastic Band (NEB) method (Henkelman et al., 2000) to find the transition path and energy barrier between an initial sharp crack and a well-defined final state (either cleavage or dislocation emission) at an applied load K_I . Results show that over some range of applied K_I the transition path for both cleavage and emission is not influenced by the spurious crack tip behavior, and the evolving emission of a dislocation loop is very similar to that observed in other systems where there are no artifacts in the potentials. Thus, the physical emission path is separated from the spurious lower-energy paths by some energetic barriers such that the physical path can be studied without artifacts. We perform free-end NEB (Zhu et al., 2007; Gordon et al., 2008) using the REPLICA package within LAMMPS (Plimpton, 1995), and visualize results using the Open Visualization Tool (OVITO) (Stukowski, 2010).

We create cracks following the K-test methodology discussed thoroughly in (Andric and Curtin, 2019). The initial sharp semi-infinite crack is created starting from a perfect lattice by imposing the atomistic displacements according to the anisotropic LEFM solution at a far-field load K_I on a planar specimen, periodic in the out-of-plane direction (Fig. 2a). The system is relaxed to an energy minimum while holding the boundary atoms (within $2r_{cut}$ of the outer limits, where r_{cut} is the cut-off distance of the potential) fixed. For cleavage, the final state corresponds to a sharp crack that has advanced one periodic distance along the crack growth direction at the same applied load K_I with boundary conditions determined by the initial state crack position (Fig. 2b). There is a small error in the elastic energy (1–3%) due to the finite simulation size (Appendix A.1) that leads to a small increase in the simulated value of K_{Ic} . For emission, the final state is a blunted crack tip with the emitted dislocation far from the crack tip (Fig. 2c). Since emission is not preferred ($K_{Ic} < K_{Ie}$), the final blunted crack tip is created by using the minimum periodic length along the crack front, which artificially reduces the energy barrier for emission significantly, followed by a molecular dynamics simulation with atoms around

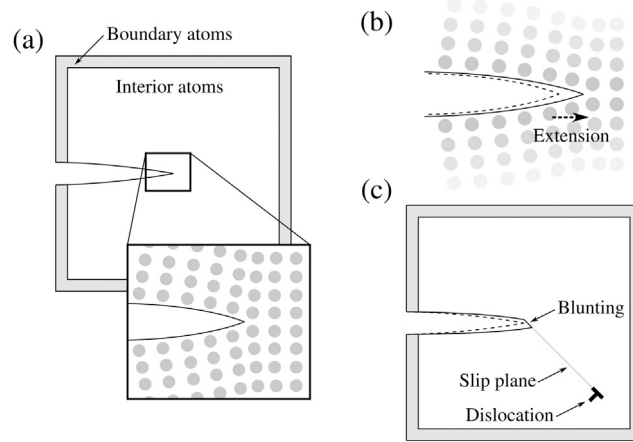


Fig. 2. Schematic of the K -controlled simulation setup in the x - y plane. The specimen has periodic boundary conditions along the crack front in the out-of-plane direction. (a) Initial configuration of the semi-infinite crack tip (b) Uncracked (dashed line) and cracked configurations of the crack for the cleavage NEB simulations; the crack tip remains sharp after cleavage. (c) Sharp crack before emission (dashed line) and blunted crack after emission configurations for the dislocation emission NEB simulations.

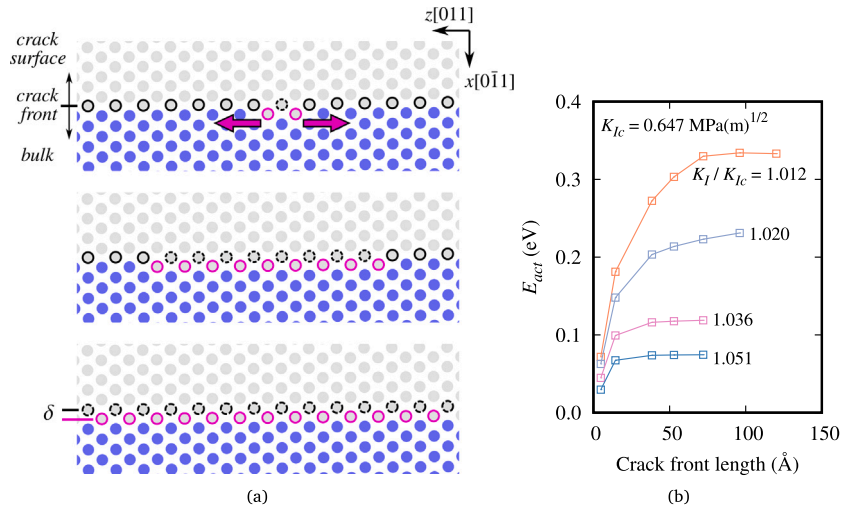


Fig. 3. NEB simulation of the cleavage process in NbTiZr for the 110/112 crack orientation. (a) A small section of decohered atoms along the crack front (outlined in purple) expands laterally across the crack front until the crack front line has advanced by one periodic spacing δ . Atoms are colored by structure according to Common Neighbor Analysis: bcc (blue), non-bcc surface atoms (white). (b) The energy barrier versus crack front length at varying K_I (labels indicate K_I/K_{Ic}), showing the full 3d barrier to be achieved for a crack length of $\sim 70\text{\AA}$.

the crack tip at temperature $T \gg 0$ to induce emission. The final $T = 0$ blunted crack tip is then obtained by cooling the specimen to $T = 0$ and replicating the structure along the crack line direction to create the full final-state 3-d specimen for the NEB simulation.

The cleavage and emission processes are intrinsically 3d, as revealed by the NEB simulations. As shown in Fig. 3(a), cleavage involves the formation of a small section of decohered atoms just ahead of the original crack tip that then expands laterally along the entire (periodic) crack front, advancing the entire crack front line by one lattice spacing. The energy barrier at an applied K_I above K_{Ic} but below the zero lattice trapping barrier corresponds to some critical length of decohered atoms. Dislocation nucleation below K_{Ic} is an instability due to the nucleation of a finite-sized loop on the slip plane that then expands out both laterally and ahead of the crack until a full dislocation line is formed, which then moves away from the crack tip (Fig. 4(a)). The energy barrier at an applied $K_I < K_{Ic}$ corresponds to some critical loop size. Since bcc dislocations do not dissociate into partials, the slipped region behind the emitting dislocation loop has the perfect bcc crystal structure. The two 3d processes of cleavage and emission thus require simulations on sufficiently thick specimens (crack front lengths) to capture the true 3d energy barrier. Figs. 3(b) and 4(b) show the energy barriers for both cleavage and emission as a function of crack front length; only the asymptotic results at larger crack front lengths ($\sim 70\text{\AA}$ in depth) have physical meaning and are the only results quoted below.

The energy barriers for cleavage and emission versus K_I as computed using the free-end NEB method and the average-atom EAM potentials for four HEAs over a range of K_I are shown in Fig. 5 for the most ductile orientation studied here, i.e. 110/112.

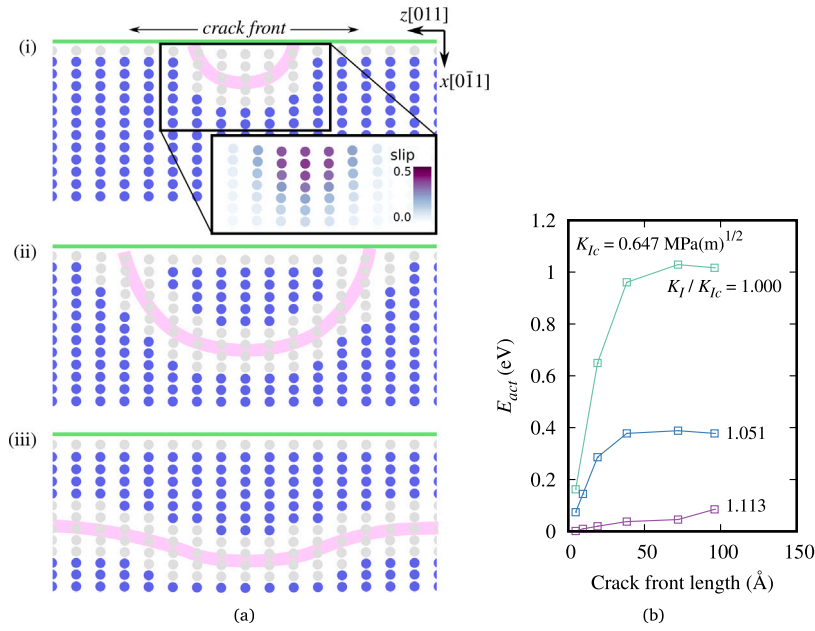


Fig. 4. NEB simulation of the dislocation emission process in NbTiZr for the 110/112 crack orientation. (a) Behavior of the emitting dislocation loop at $K_{Ic} = 0.647 \text{ MPa}\sqrt{\text{m}}$. Atoms are colored by structure according to Common Neighbor Analysis: bcc (blue), non-bcc atoms (white). A pink line is provided to show an approximate configuration of the dislocation loop. (i) The critical loop configuration is indicated by the white atoms. The slip inside the loop area (see inset) is less than the Burgers vector b . (ii) Unstable bow-out of the loop across the crack front after the critical configuration. (iii) An eventually straight dislocation moves away from the crack tip. (b) The energy barrier versus crack front length at varying K_I (labels indicate K_I/K_{Ic}) showing the full 3d barrier to be achieved for a crack length of $\approx 50 \text{ Å}$.

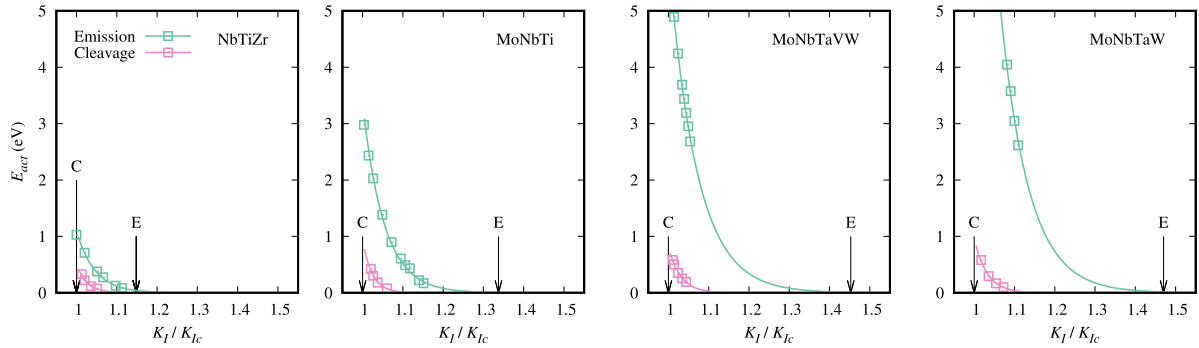


Fig. 5. Energy barriers for cleavage and dislocation emission in the 110/112 crack orientation as a function of the applied load K_I . A fit of the form $E_{act} = b \exp(aK_I/K_{Ic})$ is shown (a and b are fitting coefficients). The extrapolated barrier becomes very small close to the LEFM prediction of K_{Ic} . The LEFM $T = 0 \text{ K}$ critical stress intensities are indicated by arrows and labels C= K_{Ic} and E= K_{Ic} .

The cleavage results show a fairly small lattice-trapping barrier (less than $\approx 0.5 \text{ eV}$) at the LEFM-predicted K_{Ic} . The cleavage barrier decreases quickly for $K_I > K_{Ic}$, reaching essentially zero at K_I less than $1.1 K_{Ic}$. This behavior is due to the well-established lattice trapping phenomenon (Thomson et al., 1971; Curtin, 1990). Since there is some barrier for cleavage at K_{Ic} , cleavage can require slightly higher loads depending on temperature, time, and crack front length (cleavage can nucleate anywhere along a long crack front). The emission barrier increases with decreasing $K_I < K_{Ic}$. The NEB results are limited to some maximum K_I above which the transition path exhibits behavior that invalidates the use of the computed barrier. At any K_I , however, the emission barrier is always larger than the cleavage barrier, and becomes insurmountably large (2–3 eV) at values of K_I still well above K_{Ic} . Therefore, for $K_I > K_{Ic}$, the rate of thermally-activated cleavage is always much higher than emission. Thermal activation therefore does not change the underlying brittleness of these refractory HEAs as represented by the model EAM potentials.

The NEB results enable some validation of K_{Ic} for these bcc alloys, as follows. The material properties entering into analytic theory (elastic constants, surface energy and USF energy) are determined fully by the interatomic potential. The computed NEB energy barriers are fit to the functional form $E_{act} = b \exp(aK_I/K_{Ic})$ with a and b fitted parameters. The LEFM value of K_{Ic} does not enter into this fitting. Nonetheless, we find that the extrapolated emission barriers are indeed predicted to become very small

Table 1

Material parameters of bcc refractory elements used in the LEFM analysis: the elastic constants C_{ij} , the relaxed surface energies γ_s and unstable stacking fault energies γ_{usf} . The Zener anisotropy ratio $a_r = 2C_{44}/(C_{11} - C_{12})$ is computed. The anisotropy parameter χ is also shown for all combinations of crack and emission planes, showing deviations relative to the isotropic values shown in Fig. 1.

Element	C_{11}	C_{12}	C_{44}	a_r	Plane	γ_s	γ_{usf}	χ	
	GPa					J/m ²		110	112
Mo	450	173	125	0.90	100	3.250	–	2.416	2.433
					110	2.834	1.389	2.242	1.957
					112	–	1.390	–	–
Nb	253	133	31	0.52	100	2.310	–	2.233	2.287
					110	2.058	0.637	2.088	1.918
					112	–	0.752	–	–
Ta	266	158	87	1.62	100	2.490	–	2.715	2.827
					110	2.352	0.719	2.486	1.951
					112	–	0.829	–	–
V	238	122	47	0.81	100	2.381	–	2.233	2.282
					110	2.404	0.693	2.091	1.923
					112	–	0.793	–	–
W	533	241	199	1.37	100	4.026	–	2.529	2.576
					110	3.282	1.692	2.336	1.945
					112	–	1.714	–	–

(emission at essentially $T = 0$ K) quite close to the LEFM-predicted K_{Ie} (indicated in Fig. 5). Thus, the NEB study demonstrates that the LEFM-predicted K_{Ie} is a good estimate of the zero-barrier emission load.

These results show that the $T = 0$ K LEFM values of K_{Ic} for cleavage and K_{Ie} for emission are accurate. These atomistic studies show that thermal-activation effects can be largely neglected because, for brittle alloys where $K_{Ic} < K_{Ie}$, the cleavage barriers for $K_I > K_{Ic}$ are small and the emission barriers for $K_I < K_{Ie}$ are usually much larger than the cleavage barriers. The LEFM theory is thus used throughout the remainder of the work presented here.

3. Ductility criterion based on intrinsic fracture of bcc elements

The stable low temperature crystal structures of the refractory elements Mo, Nb, Ta, V, and W are bcc. The elements Ti and Zr that will later appear as constituents in various HEAs have an hcp structure at low temperatures and are only stable in the bcc structure at high temperatures or via alloying at low temperatures. We thus only consider Mo, Nb, Ta, V, and W here.

Fully-relaxed values of γ_s for the {100} and {110} surfaces and γ_{usf} for the {110} and {112} planes have been computed using DFT as implemented in VASP for the five elements of interest. Appendix A.3 provides important details about these computations. The elemental elastic moduli are also required, but it is well-established that the DFT-computed value of C_{44} is in poor agreement with experiments (Koči et al., 2008) (also see Appendix A.2). Here, we therefore use the experimental elastic moduli (Featherston and Neighbours, 1963; Carroll, 1965; Bolef et al., 1971). The relevant material parameters are shown in Table 1.

As a first validation of the material parameters computed here, we compute the brittle fracture toughness of W in the 100/110 crack orientation to be $K_{Ic} = 1.950 \text{ MPa}\sqrt{\text{m}}$. The single-crystal fracture toughness data measured at 77 K, independent of the strain rate, is $(2.7 \pm 0.2) \text{ MPa}\sqrt{\text{m}}$ (Giannattasio and Roberts, 2007). Extrapolating the fracture toughness data measured over many samples over a range of temperatures (see Fig. A.2) yields $K_{Ic} = 2.198 \text{ MPa}\sqrt{\text{m}}$. This agreement is good, well within the uncertainty of the extrapolation. Macroscopic experimental toughness also typically exceeds the theoretical K_{Ic} even in very brittle materials due to the formation of ledges/steps along the crack front and other defects. Such effects do not change the fundamental competition between cleavage and emission at the sharp crack tip, however.

Fig. 6(a) shows the computed K_{Ic} and K_{Ie} values for the 5 bcc elements studied here for all four orientations. The ductility index is $D = K_{Ie}/K_{Ic} > 1$ for all these metals over all four orientations (Fig. 6(b)). This is in agreement with the experimentally-established brittleness of all of these metals at very low temperatures. Each element has a brittle-to-ductile transition over a relatively narrow window of temperature typified by the Brittle-to-Ductile Transition Temperature (BDTT). We are interested in RT ductility, which is often characterized in terms of reduction of area at fracture. Ductile materials show a large reduction in the cross-sectional area prior to failure while brittle materials will fracture with little to no change in the area. In Fig. 6(c), experiments at RT show that Nb, V, and Ta reach an area of reduction at fracture of $> 90\%$ (BDTT $<$ RT) (Spitzig and Owen, 1987). These elements are considered fully ductile since they show area reductions similar to conventional ductile elements, e.g. Ni (Northcott, 1961). By the same measure, Mo becomes ductile around RT (BDTT \sim RT) and W is brittle at RT (BDTT \gg RT) (Northcott, 1961). Also shown in Fig. 6(c) are the deduced BDTT from other experiments (Joseph et al., 2007; Roberts et al., 1993; Giannattasio and Roberts, 2007), which are consistent with data on area reduction. The relative ductility as represented by the ductility index D computed from the DFT-based LEFM is $D(\text{Nb}) < D(\text{V}) \sim D(\text{Ta}) < D(\text{Mo}) < D(\text{W})$, which is qualitatively consistent with the RT experimental trends and the ordering of the BDTT values.

Our analysis shows that D is systematically lower (toward more ductile) for the 100/110 orientation on {100} fracture plane and the 110/112 orientation on the {110} fracture plane. Since any cleavage must be possible on the most ductile orientation of any

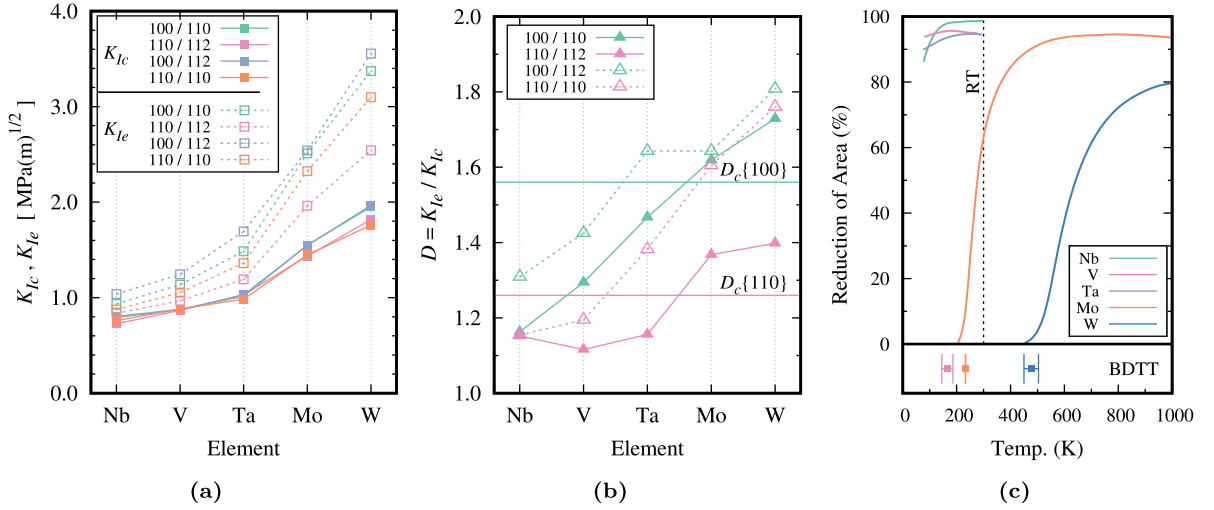


Fig. 6. (a) LEFM predictions of K_{Ic} (solid lines) and K_{IIc} (dashed lines) for 5 bcc elements and four crack orientations, using DFT-computed surface and USF energies and experimental elastic moduli; (b) Predicted ductility index $D = K_{IIc}/K_{Ic}$ for all cases. The proposed critical values $D_c\{110\} \approx 1.26$ and $D_c\{100\} \approx 1.56$ are also shown, selected to capture the experimental RT behavior (ductile or brittle); (c) Experimental reduction in cross-section area at tensile failure as a measure of RT ductility and the DBTT, from selected sources (see main text).

fracture plane, it is the 100/110 and 110/112 orientations that control the ductility according to the intrinsic fracture criterion. In subsequent sections, we will therefore study these two orientations in depth.

We now address how we use the ductility index D computed at $T = 0$ K to understand ductility at RT. As noted, $D < 1$ is not satisfied by any of the elements, consistent with low- T experiments, but all elements do have a DBTT at higher temperatures. The ductility index does not predict a DBTT, and it is highly unlikely that the use of temperature-dependent material properties of refractory elements at RT will alter the K_{IIc}/K_{Ic} sufficiently to reach $D < 1$. To proceed, we therefore use the experimental observations of RT ductility to select a critical value of the ductility index D_c (one value for each cleavage plane) that captures the experiments. From Fig. 6(c), the RT experimental ductility observed in Nb, V, and Ta is clearly distinct from the absence of RT ductility in W. The ductility of Mo transitions around RT, but the exact conversion between the area of reduction to ductility is not well-defined. We conservatively select $D_c\{110\} \approx 1.26$ and $D_c\{100\} \approx 1.56$ to capture RT ductility in Nb, V, and Ta and relatively lower ductility in Mo and W, as shown in Fig. 6(b). Ductility is only achieved if $D < D_c$ is satisfied for *both* fracture planes.

The selected RT D_c values represent a correlation only, and are larger than unity. The result of $D > 1$ for all the elements is consistent with very early estimates of Ohr (Ohr, 1985). There are several reasons why ductility (crack tip emission) could arise at finite T for $D > 1$ at $T = 0$ K. First, as discussed by Ohr, small amounts of mode II and/or mode III loading of the appropriate sign can facilitate emission relative to cleavage, reducing D . With isotropic elasticity, the effects of mode II and mode III loading can be assessed easily (also see Appendix A.4), and the ductility index of the mixed-mode loading D^{mix} derived as

$$\frac{D^{mix}}{D} = \frac{\sqrt{1 + \left(\frac{K_{II}}{K_I}\right)^2 + \frac{1}{1-\nu} \left(\frac{K_{III}}{K_I}\right)^2}}{1 \pm \frac{K_{II}}{K_I} \left(2 \csc \theta - 3 \tan \frac{\theta}{2}\right) \pm 2 \frac{K_{III}}{K_I} \csc \theta \tan \phi} \quad (5)$$

The ductility ratio still scales with the mode I ductility ratio, i.e. it still depends on the ratio of the USF energy and surface energy, but now also on the magnitude and sign of the mixed mode components. Fig. 7 shows the fractional reductions in D for the most favorable signs of the mixed mode loadings for all four crack orientations in two cases ($K_{II}/K_I = \pm 0.1$; $K_{III} = 0$) and ($K_{II}/K_I = K_{III}/K_I = \pm 0.1$). In the latter case, $D_c\{110\}$ is reduced by $\approx 10\%$, bringing it close to unity while $D_c\{100\}$ is reduced by $\approx 30\%$, also bringing it close to unity. Particularly in polycrystals, this level of mode mixity for cracks best-oriented for mode I loading is modest. This would be the most likely explanation for ductility based on a purely mode I D_c . Second, some dislocation motion around the crack may also create additional mode II or mode III contributions, aiding ductility. Third, recent work on the double-kink nucleation barrier for screw dislocation motion in W has shown that anharmonic effects lower the barrier even at 400–600 K, and hence anharmonic effects may play a role in crack tip nucleation as well (Swinburne and Marinica, 2018). The latter two factors are beyond the scope of the present work. We show below that use of the selected values of D_c based on mode I analysis, although larger than unity, enables predictions of ductile and brittle behavior across a range of HEAs consistent with experimental observations to date.

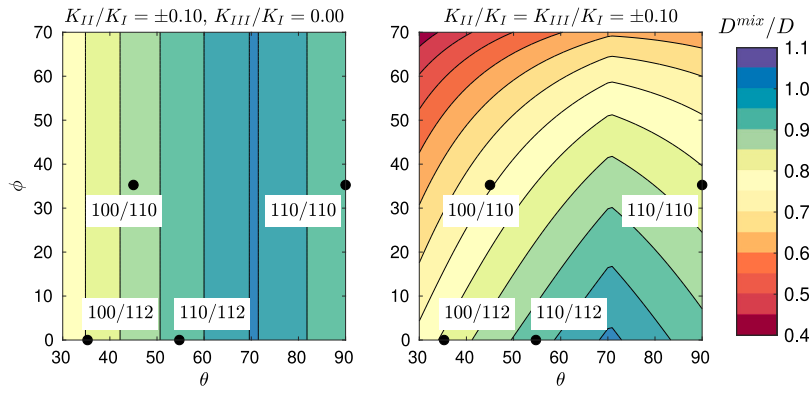


Fig. 7. Mixed-mode isotropic ductility index normalized by the pure mode I ductility index for the various possible dislocation emission slip planes studied here (see Eq. (5)). The kinks in the graphs arise due to changes in the signs of the mixed mode components that reduce the ductility index.

4. Ductility in high entropy alloys

4.1. Ductility of MoNbTaVW, MoNbTaW, and MoNbTi using first-principles inputs

For random HEAs, we use the same theoretical framework as applied to the elements but now using the average macroscopic properties of each alloy. Here, we first apply the LEFM theory to the equiatomic MoNbTaVW, MoNbTaW and MoNbTi HEAs using first-principles DFT material properties.

The theory requires the elastic constants, but in fact only requires the anisotropy ratio that enters the χ parameter. To our knowledge, there are no experimental studies of the elastic constants of these alloys beyond the polycrystalline averages, and hence no information on elastic anisotropy. As for the elements, DFT studies underestimate C_{44} (Maresca and Curtin, 2020a). The Zhou et al. EAM interatomic potentials were designed/fitted to the various bcc elements and so provide very good results for the alloys (see Appendix A.2). Specifically, the lattice constants agree well with experiments and both C_{11} and C_{12} agree well with DFT values. The C_{ij} including C_{44} obtained for the HEAs for the alloys are then also consistent with subsequent estimates of the polycrystalline moduli of the real alloys. We use the elastic constants predicted from these EAM potentials for the present HEAs, remembering that the predictions of D only depend on the elastic anisotropy and not on the absolute values of the elastic constants.

The theory also requires the surface and USF energies. We have computed the relaxed values for the various HEAs using first-principles DFT as implemented in VASP. We use large Special Quasi-random Structures (SQS) and examine several random realizations for some alloys. The computation of the USF energy requires some care due to the fact that atoms do not sit exactly on the ideal lattice sites in the bulk crystal. The details of our DFT methodology are discussed in Appendix A.3. Our results for the surface and USF energies are shown in Table A.4. Also shown are recent results by (Li et al., 2020) for two alloys obtained using the very different first-principles CPA-EMTO methodology that usually provides results in reasonable agreement with standard DFT implementations.

The DFT predictions for MoNbTaVW, MoNbTaW, and MoNbTi are shown in Fig. 8(c). Classification of these HEAs as brittle or ductile according to our RT criterion $D_c\{100\}$ and $D_c\{110\}$ shows agreement with experimental ductility trends. MoNbTaVW and MoNbTaW are predicted to be brittle since $D > D_c$ for both orientations. Correspondingly, Senkov et al. (2011b) show that polycrystalline MoNbTaVW and MoNbTaW are quite brittle in RT compression with $< 3\%$ ductility. MoNbTi is predicted to be very close to the embrittlement criterion while experiments show moderate compression ductility. The predictions using the data of Li et al. (2020) are also shown and are comparable, but higher than, our results for the 110/112 orientation but much lower for the 100/110 orientation, showing the need for standard DFT methods.

4.2. Ductility using scaled inputs from interatomic potentials

While the LEFM analysis requires only a few input parameters, the computational cost of fully-relaxed DFT studies on large SQS structures is significant and currently prohibitive for exploring many alloy compositions. Hence, here we seek an approximate approach that enables rapid assessment of many alloys. The approximate approach uses material parameters obtained by *scaling* the surface and USF energies predicted by the Zhou et al. EAM interatomic potentials (Zhou et al., 2001) to our DFT results on several alloys. We then apply a scaling factor β to scale the EAM parameters for a much wider range of HEA compositions and make predictions of ductility using these scaled EAM inputs.

The Zhou et al. family of EAM potentials were fit to basic material properties (e.g. cohesive energy, lattice constants, elastic constants) but not to surface or USF energies. Thus, we first examine the predictions of these potentials for γ_s and γ_{usf} for the elements and for selected HEAs for which we have DFT data. Fig. 8(a) shows the ratio of fully-relaxed EAM to fully-relaxed DFT surface and USF energies for the elements Mo, Nb, Ta, V, and W. The EAM potential systematically underestimates the surface energies, with $\gamma_s^{\text{EAM}} \approx 0.8\gamma_s^{\text{DFT}}$. In contrast, the estimation of γ_{usf} by the EAM potential ranges from $0.8 - 1.2\gamma_{usf}^{\text{DFT}}$.

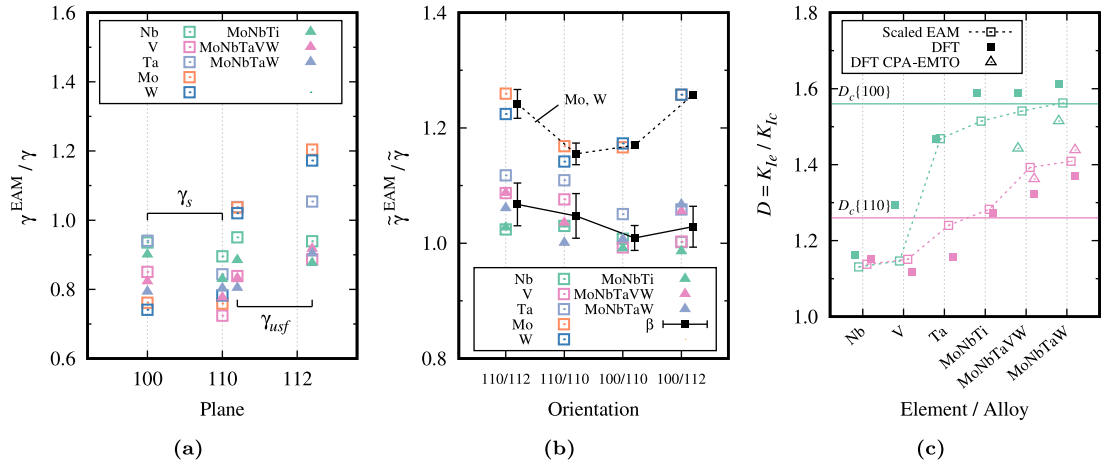


Fig. 8. Fully-relaxed EAM material properties compared to fully-relaxed DFT material properties. (a) Ratio of EAM to DFT surface energy γ_s and USF energy γ_{usf} for several bcc elements and the MoNbTi, MoNbTaVW, and MoNbTaW HEAs. (b) Ratio of energies $\tilde{\gamma} = \sqrt{\gamma_{usf}/\gamma_s}$ entering the ductility analysis. The elements Mo and W stand out from among the other elements and the two HEAs due to the higher values of the USF for the EAM potential shown in (a). The average values for Nb, Ta, V, MoNbTi, MoNbTaVW, and MoNbTaW are shown, and are used as a scaling factor β (see text). (c) Comparison of scaled EAM ($\beta = 1.04$) versus DFT predictions of ductility for Nb, V, Ta, MoNbTi, MoNbTaVW, and MoNbTaW; some symbols slightly offset for visual clarity.

EAM results for the hcp elements Ti and Zr (not shown) deviate significantly from DFT for the {110} surface energies ($\sim 40\%$) and USF energies ($\sim 80\%$). This is likely due to both inaccuracy of $T = 0$ K DFT for bcc Ti and Zr as well as inaccuracy of the EAM potentials that were fit to the hcp properties rather than to the bcc properties. We can thus expect that alloy compositions with high Ti and/or Zr content will be poorly described by the EAM potentials. With the exception of NbTiZr, we therefore avoid the study of alloys with Zr and restrict the Ti composition to 33.33% at most.

Fig. 8(b) shows the ratio of EAM to DFT values for the quantity $\tilde{\gamma}$ that enters the ductility condition. For the elements Nb, Ta, V, and HEAs MoNbTi, MoNbTaVW, and MoNbTaW, the ratios fall in a fairly narrow range. The ratios for elemental Mo and W are much higher, but these elemental deviations are not reflected in the values for the HEAs containing Mo and W up to 50% of the composition. Since even the MoNbTaVW and MoNbTaW alloys are observed and predicted to be brittle, alloys with higher Mo and W content are also likely to be quite brittle. We therefore consider scaling of EAM results to DFT results using the results for Nb, Ta, V, MoNbTi, MoNbTaVW, and MoNbTaW. For these materials, the energy ratio falls in a narrow range across all four orientations. We thus introduce a single scaling factor β relating the EAM energy ratio to the DFT energy ratio as

$$\beta = \frac{\sqrt{\gamma_{usf}^{EAM}/\gamma_{usf}}}{\sqrt{\gamma_{usf}^{EAM}/\gamma_s}} = \frac{\tilde{\gamma}^{EAM}}{\tilde{\gamma}} \quad (6)$$

averaged across all four orientations, leading to $\beta = 1.04 \pm 0.03$ with variations of $\pm 3\%$. The ductility index D for any alloy is then estimated using the EAM values for the alloy scaled by the factor β as

$$D = \frac{1}{\beta} D^{EAM} \quad (7)$$

Fig. 8(c) compares the estimated ductility indices using the scaled EAM data against the actual DFT-based predictions for Nb, V, Ta, MoNbTaVW, and MoNbTaW. The agreement is generally good, preserving the ductility trends across these metals. As an aside, if the same β factor was applied to Mo and W, they would be predicted to be even less ductile than found using the DFT results.

We now apply the same procedure and scaling factor $\beta = 1.04 \pm 0.03$ to a wider range of HEA compositions. Fig. 9 shows the estimated ductility ratios for both orientations for a range of HEAs studied experimentally, with the $\pm 3\%$ uncertainty in β indicated. The available experimental data on ductility (maximum strain in compression) is also shown (Corry et al., 2019; Senkov et al., 2018, 2019; Chen et al., 2014; Liaw, 2020; Yao et al., 2016a,b), where arrows indicate experiments that were not continued until failure. The predictions across this scope of alloys fall into three categories: ductile ($D < D_c$ for both orientations), borderline ductile ($D \approx D_c$ for one orientation and $D < D_c$ for the other orientation) and brittle ($D > D_c$ for at least one orientation).

The Nb-rich alloys Nb₇Mo_{1.4}Ti_{1.8}, Nb_{6.8}Mo_{1.4}Ti_{1.8}, are all predicted and observed to be ductile (over 50% strain). The NbTiZr alloy is also ductile but the prediction is approaching the borderline for the 100/110 orientation due to an erroneous large USF energy predicted by the EAM potential that is $\sim 20\%$ higher than the *unrelaxed* DFT value; more accurate results should predict that this alloy is ductile, as observed. The alloys AlNbTaTi and NbTaTiV satisfy the ductility criteria and exhibit failure strains of over 25% and 50%, respectively. NbTaTi is also predicted to be ductile, but data extends only to 15% strain (but with no indication of impending failure). MoNbTi, MoNbTaTi, MoNbTiV, NbTaTiVW, NbTaTiW and MoNbTaV, with 25% or more of the brittle elements Mo and W, have failure strains of $\approx 25\%$ in compression and are predicted to be borderline ductile; their tensile ductility is likely low but not negligible. The 25% Cr alloys CrMoTaTi, CrMoNbTi, and CrMoNbV, which also contain 25% Mo, are predicted to

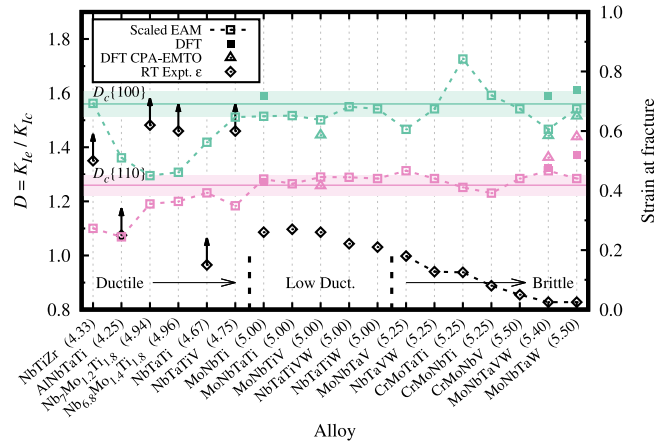


Fig. 9. Predicted intrinsic ductility index $D = K_{Ic}/K_{Ic}$ and measured RT compression ductilities for selected HEA compositions. Experimental data with arrows indicate that tests were not carried out to the ductility limit. Predictions shown mainly use scaled EAM properties with the scaling factor $\beta = 1.04$, but results using fully-relaxed DFT properties and by CPA-EMTO DFT of (Li et al., 2020) are shown where available. The RT ductility criterion for each cleavage plane is $D_c\{110\} \approx 1.26 \pm 3\%$ and $D_c\{100\} \approx 1.56 \pm 3\%$ as indicated. The alloy Valence Electron Count (VEC) is shown along with the alloy composition. Experimental data from (Senkov et al., 2018) (NbTiZr), (Coudry et al., 2019) (AlNbTaTi, NbTaTi, MoNbTaTi, NbTaTiW, CrMoTaTi, CrMoNbTi), (Senkov et al., 2019) (Nb₇Mo_{1.2}Ti_{1.8}, Nb_{6.8}Mo_{1.4}Ti_{1.8}, MoNbTi), (Chen et al., 2014) (MoNbTiV), (Liaw, 2020) (CrMoNbV), (Yao et al., 2016a) (MoNbTaV), and (Yao et al., 2016b) (NbTaTiV, NbTaTiVW, NbTaVW).

be borderline or brittle, and exhibit fracture in compression at strains under 15%. The two Senkov et al. alloys MoNbTaVW and MoNbTaW are brittle as discussed earlier.

Our results above identify several general concepts. For the Senkov et al. alloys, the small differences between DFT and EAM-scaled results can put the alloys further or closer to the ductility limits. Thus, for alloys where the EAM-scaled results are close to the ductility criteria, more accurate DFT studies should be performed. Alloys predicted to be clearly ductile, i.e. those well below D_c for both orientations, are candidates for fabrication and testing. However, alloys near the ductility criteria, i.e. within the range of D_c , have uncertain ductility but may also be worth exploring if they are expected to have other attractive properties. Lastly, the ductility criteria D_c are not definitive, and hence improved correlations with experiments may emerge by using slightly different values for $D_c\{110\}$ and/or $D_c\{100\}$.

5. Identifying new ductile HEA compositions

In previous sections, we have shown that (i) the LEFM theory is validated by atomistic simulations, (ii) ductility criteria can be established based on first-principles versus experimental data on the refractory elemental metals, (iii) trends in ductility across a few alloys can be captured by first-principles material properties, and (iv) trends in ductility across even more HEAs studied to date can be reasonably captured by using the scaled EAM material properties. We can thus now use the LEFM theory, the ductility criteria, and the scaled EAM properties to make predictions for ductility across a much wider range of alloys with the goal of identifying promising new alloys for fabrication and testing.

Here, we investigate three families of alloys: Mo-Nb-Ti with Ti $\leq 33.33\%$, Mo-Nb-Ta-V-W with Mo = 0.20 to reduce the space of compositions, and Mo-Nb-Ta-W. Fig. 10 shows the predicted ductility indices versus alloy composition for these three families. The ductility index is normalized by the critical value for each orientation ($D\{110\}/D_c\{110\}$ and $D\{100\}/D_c\{100\}$). Using the uncertainty range in D_c of $\pm 3\%$ due to scaling, a ductile alloy has both normalized indices less than 0.97 (both entries colored green in Fig. 10).

Mo-Nb-Ti is predicted to be ductile when the Nb content is high ($\geq 50\%$) and the Mo content is low ($< 20\%$), and brittle when the Mo content is $\geq 30\%$, following the trends toward ductile Nb and brittle Mo (Fig. 6(b)). We do not show results for Ti content exceeding 33% but increasing Ti content decreases ductility in 100/110 but increases ductility in 110/112. The Mo_{0.2}Nb_{0.5}Ti_{0.3} alloy might be an attractive candidate for preserving high strengths and achieving improved ductility over MoNbTi.

Mo_{0.20}-Nb-Ta-V-W has no truly ductile domains, which is unfortunate since high strength retention at high T is most likely found in the Mo-Nb-Ta-V-W space. However, some cases are borderline for sufficiently low W content and with higher Nb content tending toward ductility, consistent with Nb typically being the most ductile of the elements. For instance, Mo_{0.2}Nb_{0.3}Ta_{0.3}V_{0.2} might be more attractive for ductility than MoNbTaVW. Similarly, Mo-Nb-Ta-W becomes ductile only as the Mo and W content is minimized (combined 20%) with the most ductile composition maximizing Nb, i.e. Mo_{0.10}Nb_{0.70}Ta_{0.10}W_{0.10}. Overall, the ductility of an alloy generally reflects the ductility of the constituent elements (i.e. from Fig. 6(b)) in rough proportion to their concentrations. However, we have found that rule-of-mixtures approaches to estimating material properties are not highly accurate.

The dimensionality of an N -component can be reduced to one generalized coordinate of the average valence electron count (VEC) of the alloy. Yang and Qi (2018) have proposed that, in the context of binary W-Ta and W-Re alloys, D is maximized around VEC = 5.8. Li et al. (Li et al., 2020) suggested that intrinsic ductilization, i.e. $D < 1.0$, may be possible on {110} for VEC < 4.2 .

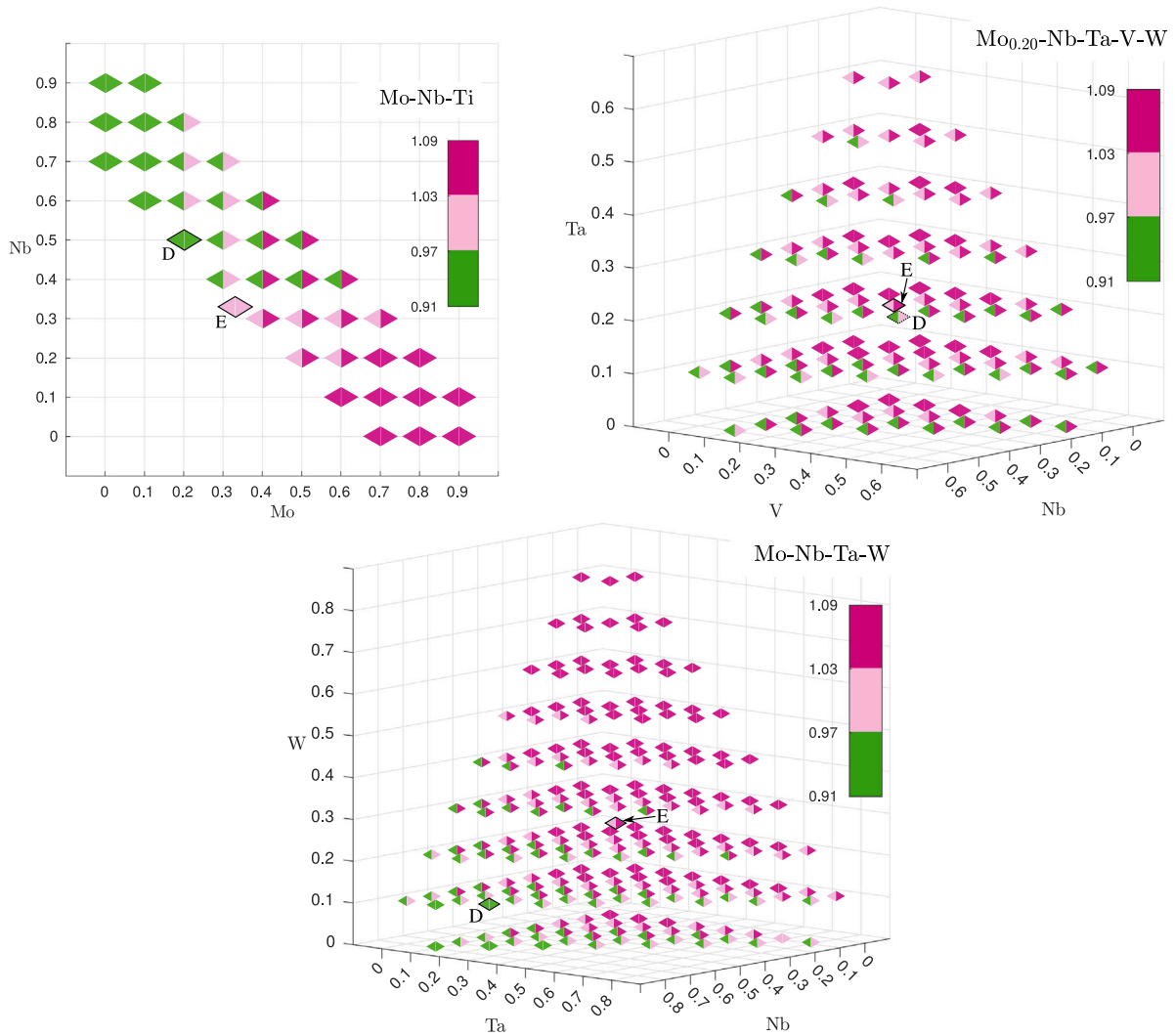


Fig. 10. Ductility for three HEA families discretized at intervals of 10% concentration of each alloy constituent, using scaled EAM properties ($\beta = 1.04$). For each composition, the ductility of the 100/110 (\blacktriangleleft symbols) and 110/112 (\blacktriangleright symbols) orientations are normalized by the critical values $D_c\{100\}$ and $D_c\{110\}$, respectively. Light pink color corresponds to the borderline range of $D_c \pm 3\%$ as in Fig. 9. A RT ductile alloy has both normalized indices colored green. The equicomposition alloy and the closest ductile composition to it for each family are labeled “E” and “D”, respectively. For Mo-Nb-Ti, only compositions with Ti $\leq 33.33\%$ are shown.

These are consistent with the trends here. We pursue this idea further here by recasting our results in Fig. 10 into the reduced space of D versus VEC as shown in Fig. 11 for the two critical orientations 110/112 and 100/110. For the 100/110 orientation, we find a wide range of D at fixed VEC for Mo-Nb-Ti (Ti < 0.33), $\text{Mo}_{0.20}\text{-Nb-Ta-V-W}$, and Mo-Nb-Ta-W alloys, spanning above and below the critical D_c . Importantly, there is thus no distinct correlation between alloys with $D < D_c$ and any critical value of VEC. However, many alloys with VEC < 5.25 have $D < D_c$ for this orientation. For the 110/112 orientation, there is a much cleaner, roughly linear, correlation between D and VEC over the entire range of $4 < \text{VEC} < 6$. A similar linear trend for $\{110\}$ cracks is noted by Li et al. (2020). There remains a spread in D values at any VEC, but nearly all alloys with VEC < 5.0 fall into the ductile $D < D_c$ regime for this orientation.

According to Fig. 11, our RT ductility criteria appear to correlate with VEC < 5.0 . In Fig. 9, the alloys with VEC = 5.0 are borderline whereas those with VEC < 5.0 are ductile. However, we predict (not shown) that NbTaV (VEC = 5.0) is ductile, which would not be surprising since the underlying elements Nb, Ta, and V are all ductile. The VEC alone thus does not appear sufficient to fully characterize ductility but we suggest use of VEC < 5.0 as a rapid first-screening for ductile compositions.

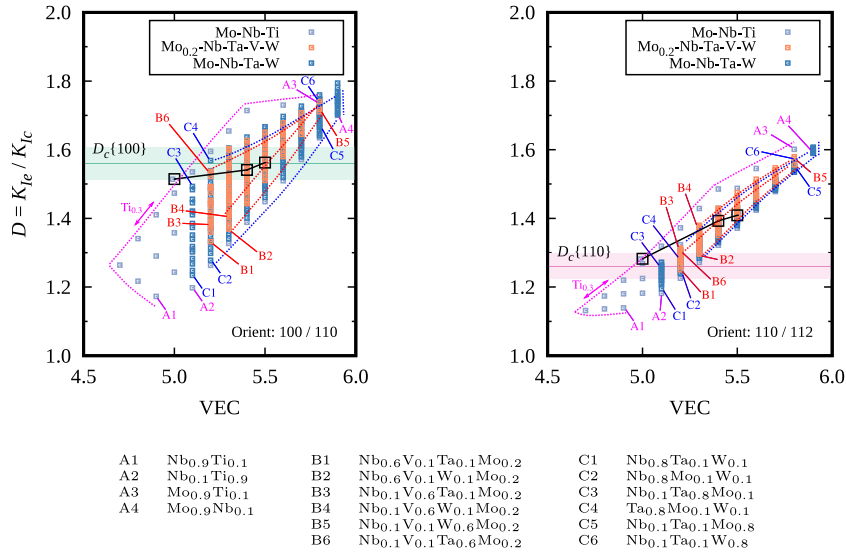


Fig. 11. Ductility index $D = K_{Ic}/K_{Ic}$ versus the average valence electron count (VEC) per atom for three HEA families corresponding to Fig. 10, with the ductility criteria indicated, for each orientation. Equiatomic compositions are indicated by the solid black line. Colored dashed lines indicate various limiting compositions.

6. Discussion

Up to this point, we have neglected the effects of temperature. Material properties entering into the fracture theory (C_{ij} , γ_s , γ_{usf}) are temperature dependent. Generally they decrease with increasing temperature, so both K_{Ic} and K_{Ie} are expected to decrease with increasing temperature. Whether or not these property changes have a significant enough effect on the ratio K_{Ie}/K_{Ic} requires more detailed knowledge of the temperature dependence of the individual material properties, which is beyond the scope of this study. We have seen in a range of alloy compositions that K_{Ie}/K_{Ic} is generally rather greater than 1. Thus, we generally do not expect these property changes in refractory alloys to lead to a change from intrinsically brittle to ductile behavior at RT. Recalling the $T = 0$ energy barriers in Section 3, thermal activation also is generally not able to change the underlying brittleness if the emission barrier is much larger and insurmountable compared to the cleavage barrier around K_{Ic} . With increasing temperature however, the emission barrier is expected to decrease slightly due to thermal activation, which may enable a cross-over from brittle to ductile in some alloys.

The mechanical strength of bcc elements is controlled by the stress- and temperature-dependent mobility of screw dislocations (Argon, 2008). Plastic flow up to moderate temperatures is dominated by the thermally-activated glide of screw dislocations. Even if a crack remains sharp, i.e. $D > D_c$, the surrounding material can be deforming due to dislocation plasticity. Dislocations in the plastic zone around a crack tip provide shielding, generally enabling a crack to support higher loads. Thus, the macroscopic fracture toughness can be significantly higher than the Griffith value even if the material remains subject to cleavage at the atomic scale. The transition to ductile behavior is here envisioned to be enabled by dislocation emission from the crack tip rather than dislocation plasticity away from the crack tip.

In HEAs, the high strength arises from strengthening mechanisms due to the random solute environment on both screw and edge dislocation glide (Maresca and Curtin, 2020a). These high strengths will naturally reduce the size of the plastic zone around a crack, and reduce the macroscopic fracture toughness. Dislocations emitted from the crack tip will also be inhibited from moving far from the crack, and thus lead to shielding of subsequent emission and possibly increased anti-shielding for cleavage, both tending to make the alloy more brittle. Here, we do not include such stochastic effects of the true randomness of the alloy because we use the statistically-averaged representation of the random alloy. However, compositional variations along the crack front will also lead to local variations in γ_s and γ_{usf} , creating local environments that are both favorable and unfavorable for cleavage/emission with respect to the average behavior. Cleavage is thermodynamic, so such local variations cannot make overall cleavage easier or harder. In contrast, dislocation emission is a nucleation event, and so can be affected by the local environment. Dislocation emission can thus occur at loads below the average K_{Ie} at regions where the local composition can facilitate emission relative to the average. A moving crack encounters many local environments, and a single emission event somewhere along the crack front can lead to blunting. Thus, randomness can also possibly improve ductility compared to the average behavior; preliminary studies of true random MoNbTi suggests this to be the case. These aspects will be considered in future work.

7. Conclusion

Low compressive ductility displayed by some bcc elements and HEAs suggests that their ductility may be related to fracture phenomena. We have thus approached ductility by analyzing the nanoscale fracture competition between cleavage and dislocation

emission at a sharp crack tip. We have validated the use of LEFM for assessing these two phenomena in selected model equiatomic HEAs described by EAM potentials. We have then used theory and experiments on bcc elements to develop a ductility criterion corresponding to critical values for the emission/cleavage ratio K_{Ic}/K_{Ie} for the two most-ductile crack orientations for bcc crystals. Application of this ductility criterion to various HEAs has then been made using material properties obtained from a validated scaling of EAM-potential properties. Generally good agreement for the predicted ductility was achieved across 18 different HEAs. The analysis was then extended to examine a much wider composition space. The same methodology can be applied to other alloy families. A correlation of ductility with Valence Electron Count was investigated as a very rapid but more-approximate assessment method. While further first-principles results will continually help refine our analysis here, such results are computationally intensive. We thus advocate application of the current methods in tandem with recent existing theories for yield strength (Maresca and Curtin, 2020a,b) to enable the computationally-guided design of strong, ductile, high temperature refractory HEAs.

CRedit authorship contribution statement

Eleanor Mak: Methodology, Investigation, Formal analysis, Writing - original draft. **Binglun Yin:** Methodology, Investigation. **W.A. Curtin:** Conceptualization, Methodology, Supervision, Writing - review & editing.

Declaration of competing interest

The authors declare that they have no known competing financial interests or personal relationships that could have appeared to influence the work reported in this paper.

Acknowledgments

This work was supported by the Swiss National Science Foundation project “Harnessing atomic-scale randomness: design and optimization of mechanical performance in High Entropy Alloys”, project “200021_18198/1”. WAC thanks Profs. L. Qi (U. Mich.) and Y.-j. Hu (Drexel) for productive discussions.

Appendix

A.1. Numerical error in NEB simulations

At Griffith cleavage K_{Ic} , the amount of relaxation of the elastic energy is exactly necessary to form new crack surface. The net energy change over the transition is zero, separated by a finite energy barrier. In the “K-test” setup, the boundary conditions for a crack configuration at a load K_I are enforced by the fixed atomic positions of the boundary atoms corresponding to the anisotropic LEFM solution with respect to a crack tip position. The boundary conditions are different for two crack configurations, both at K_I , but with different crack tip positions. However, the pair of cleavage NEB end-states require identical boundary conditions for K_I , but with the crack tip in two different positions. Thus, the relaxed energies in the two discrete systems are not exactly equal due to the constraint of the boundary condition.

A small error in residual energy at K_{Ic} is observed in the cleavage NEB simulations, i.e. $\Delta E = E(x_r = 1) - E(x_r = 0) > 0$, where x_R is the reaction coordinate of the energy profile of the MEP, which is shown for the 2d case in Fig. A.1. The magnitude of ΔE scales with the length of the crack front. However, since this error is persistent throughout all the simulation results, a rigid shift of $\sim 2\% K_{Ic}$ applied to a each set of energy barriers should not change the trends in E_{act} versus K_I .

A.2. Material parameters

The elastic moduli of selected bcc refractory elements (Mo, Nb, Ta, V, W) are shown in Table A.2. We compare the Zhou et al. (2001) EAM interatomic potential against first-principles/DFT studies and experimental literature from various sources as indicated. The $T = 0$ K experimental moduli are used in Section 3. The Zener anisotropy ($a_r = 2C_{44}/(C_{11} - C_{12})$) is calculated from the reported elastic moduli. For these elements, there is reasonable correspondence between EAM, DFT, and experiments. However, the DFT C_{44} is consistently underestimated; this is historically well-known (Kočí et al., 2008). Thus, the EAM potential provides a better description of the material anisotropy. Elements Ti and Zr, also shown in Table A.2, are hcp at low temperatures but bcc at high temperatures. It is likely that the EAM potentials that are fit to hcp properties yield spurious large anisotropy for alloys with high Ti and/or Zr content.

A similar comparison of the elastic moduli is presented for MoNbTaW, MoNbTaVW, and NbTiZr HEAs in Table A.3. The DFT value of C_{44} is also likely an underestimate for these alloys. Since the elastic moduli of the bcc refractory elements (Mo, Nb, Ta, V, W) from the EAM potential are accurate, the EAM elastic constants of MoNbTaW and MoNbTaVW are also likely accurate and supported by good comparisons of C_{11} and C_{12} versus DFT (Maresca and Curtin, 2020a). In contrast, as for Ti and Zr, the EAM-predicted anisotropy of NbTiZr is likely too large.

Giannattasio and Roberts (2007) investigated the fracture toughness of single-crystal W (see Fig. A.2). For the $\{100\}\langle 001 \rangle$ crack orientation, i.e. 100/110, a linear extrapolation of the available data ($\ln K_I$ versus T) to $T = 0$ K yields an athermal cleavage toughness of $2.198 \text{ MPa}\sqrt{\text{m}}$. In Section 3, we obtain a prediction of $K_{Ic} = 1.950 \text{ MPa}\sqrt{\text{m}}$ for W in this orientation based on DFT energies and athermal experimental elastic moduli.

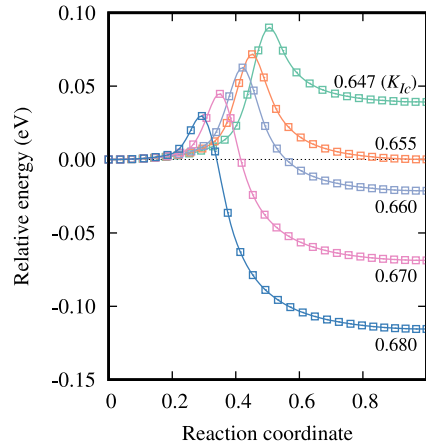


Fig. A.1. 2d cleavage energy profile of the NbTiZr 110/112 crack orientation from NEB simulation at various K_I as labeled (in units of $\text{MPa}\sqrt{\text{m}}$).

Table A.2

Elastic moduli and the Zener anisotropy of selected bcc refractory elements obtained from the EAM potential, and selected First-principles/Density Functional Theory (FP/DFT) and experimental (Expt.) literature. The Zener anisotropy ratio $a_r = 2C_{44}/(C_{11} - C_{12})$ is computed.

Element	Data	a Å	C_{11} GPa	C_{12}	C_{44}	a_r
Mo	EAM	3.150	457	167	113	0.78
	FP/DFT (Liu and Shang, 2011; Koči et al., 2008; Ikehata et al., 2004)		469	162	101	0.66
	Expt. ($T = 300$ K) (Katahara et al., 1979; Bolef and De Klerk, 1962; Dickinson and Armstrong, 1967; Davidson and Brotzen, 1968)		466	163	109	0.72
	Expt. ($T = 0$ K) (Featherston and Neighbours, 1963)		450	173	125	0.90
Nb	EAM	3.300	262	125	36	0.52
	FP/DFT (Liu and Shang, 2011; Koči et al., 2008; Shang et al., 2010; Ikehata et al., 2004; Liao et al., 2020)		246	136	15	0.27
	Expt. ($T = 300$ K) (Allard, 1969; Katahara et al., 1979; Bolef, 1961; Walker and Peter, 1977)		246	133	28	0.51
	Expt. ($T = 0$ K) (Carroll, 1965)		253	133	31	0.52
Ta	EAM	3.303	263	158	82	1.57
	FP/DFT (Nagasako et al., 2010; Koči et al., 2008; Söderlind et al., 1993)		271	161	76	1.40
	Expt. ($T = 300$ K) (Katahara et al., 1979; Bolef, 1961; Featherston and Neighbours, 1963)		265	160	82	1.57
	Expt. ($T = 0$ K) (Featherston and Neighbours, 1963)		266	158	87	1.62
V	EAM	3.026	264	119	38	0.52
	FP/DFT (Liao et al., 2020; Shang et al., 2010; Ikehata et al., 2004; Koči et al., 2008)		268	139	21	0.32
	Expt. ($T = 300$ K) (Allard, 1969; Bolef, 1961; Katahara et al., 1979; Alers, 1960; Bolef et al., 1971; Fisher et al., 1975; Magerl et al., 1976)		230	120	43	0.78
	Expt. ($T = 0$ K) (Bolef et al., 1971)		238	122	47	0.81
W	EAM	3.165	523	204	161	1.01
	FP/DFT (Bercegeay and Bernard, 2005; Koči et al., 2008)		508	206	143	0.95
	Expt. ($T = 300$ K) (Katahara et al., 1979; Bolef and De Klerk, 1962; Featherston and Neighbours, 1963; Lowrie and Gonas, 1967; Ayres et al., 1975)		524	204	160	1.00
	Expt. ($T = 0$ K) (Featherston and Neighbours, 1963)		533	241	199	1.37
Ti (bcc)	EAM	3.292	120	109	77	13.82
	FP/DFT (Liao et al., 2020; Shang et al., 2010; Ikehata et al., 2004)		91	114	40	-3.62
	Expt. ($T > 1200$ K) (Ledbetter et al., 2004)		110	93	36	4.27
Zr (bcc)	EAM	3.590	113	101	65	10.98
	FP/DFT (Liao et al., 2020; Shang et al., 2010; Ikehata et al., 2004)		83	92	32	-7.21
	Expt. ($T > 1200$ K) (Heiming et al., 1991)		100	82	38	4.86

A.3. DFT methodology

DFT computations as implemented in the VASP code (Kresse and Furthmüller, 1996) are performed using the PBE functional (Perdew et al., 1996). The core electrons are replaced by the projector augmented wave (PAW) pseudopotentials (Kresse and Joubert, 1999). The valence-electron eigenstates are expanded using a plane-wave basis set with a cutoff energy of 550 eV. In reciprocal space, a Γ -centered Monkhorst-Pack (Monkhorst and Pack, 1976) k-mesh is used with line density consistent across all geometries. The interval between the neighboring k-points along each reciprocal lattice vector is $0.04\pi \text{ \AA}^{-1}$. The first-order

Table A.3

Elastic moduli and the Zener anisotropy of the selected HEAs obtained from the EAM potential and selected First-principles/Density Functional Theory (FP/DFT) literature.

Alloy	Data	a Å	C_{11} GPa	C_{12}	C_{44}	a_r
MoNbTaW	EAM	3.221	352	174	96	1.08
	FP/DFT (Maresca and Curtin, 2020a)	3.237	374	163	64	0.61
	DFT CPA-EMTO (Li et al., 2020)		412	185	71	0.63
MoNbTaVW	EAM	3.200	310	158	83	1.10
	FP/DFT (Maresca and Curtin, 2020a)	3.192	338	164	51	0.59
	DFT CPA-EMTO (Li et al., 2020)		371	178	52	0.54
NbTiZr	EAM	3.396	148	111	61	3.36
	FP/DFT (Rao et al., 2019a)	3.390	143	96	29	1.23

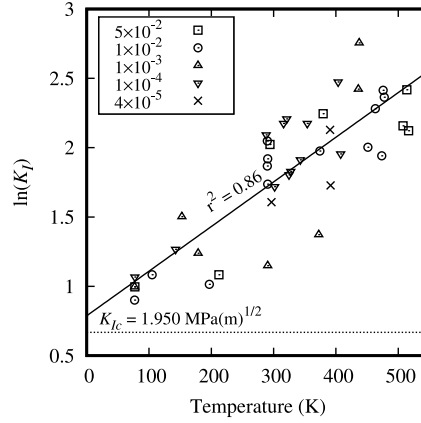


Fig. A.2. Brittle fracture toughness K_I versus temperature of W in the $\{100\}\langle 001 \rangle$ crack orientation at varying strain rates (Giannattasio and Roberts, 2007). An athermal cleavage toughness of $2.198 \text{ MPa}\sqrt{\text{m}}$ estimated by linear extrapolation to $T = 0 \text{ K}$ (solid line) shows good correspondence to the DFT-based LEFM prediction of $K_{Ic} = 1.950 \text{ MPa}\sqrt{\text{m}}$ (dashed line).

Methfessel–Paxton (Methfessel and Paxton, 1989) method is used to smear the single-particle eigenstates, with a smearing parameter of 0.2 eV . Ionic forces are relaxed to $< 3 \text{ meV } \text{\AA}^{-1}$.

To construct the HEA supercells, we first use special quasi-random structures (SQSs) (Zunger et al., 1990) (~ 100 atoms per SQS) to determine the average lattice constant a_{alloy} of the HEA. Then we use the a_{alloy} to construct the HEA bcc bulk structures with larger dimensions (360 atoms per supercell) with the plane of interest, i.e. for the stacking fault or surface, as the a_1 – a_2 plane.

The calculations of planar defects always requires fixing the in-plane lattice dimensions (a_1 , a_2) during relaxation. Given that (i) the supercell is quite large, and (ii) the USF energy and surface energy are not very sensitive to the in-plane lattices constants, we thus hold the in-plane lattices at the pristine bcc value a_{alloy} . Therefore, in the relaxation of the bulk HEA, we relax only the out-of-plane lattice a_3 to release the σ_{3j} stress components, while all atoms positions are fully relaxed. The USF and surface structures are then created based on this relaxed bulk structure.

The USF structure is created by tilting the a_3 supercell vector by the desired USF fault vector while keeping the atoms fixed in the relaxed Cartesian coordinates. Then a_3 and all the atoms are relaxed only in the direction normal to the stacking fault plane such that $\sigma_{33} = 0$, which is needed to account for inelastic displacements associated with the stacking fault (Yin et al., 2017; Andric et al., 2019). The free surface structure is created by extending a_3 in the direction normal to the surface, introducing a vacuum layer. Again, all the atoms are fixed to the relaxed Cartesian coordinates. The supercell vectors are fixed and all the atoms are fully relaxed. Our surface energies and USF energies determined according to this methodology are presented in Table A.4 along with recent results by Li et al. (2020).

A.4. Mixed-mode ductility criterion

The addition of mode II and/or mode III shear loading affects the critical stress intensities for cleavage and emission. The thermodynamics in mixed-mode cleavage considers the total energy release rate of the mixed-mode loading, i.e.

$$G \equiv \frac{(1 - \nu)(K_I^2 + K_{II}^2) + K_{III}^2}{2\mu} \quad (\text{A.1})$$

Table A.4

Surface energies γ_s and USF energies γ_{usf} used in the LEFM analysis of four equiatomic HEAs. Energies are reported in units of J/m².

Alloy		DFT	DFT CPA-EMTO (Li et al., 2020)	EAM
NbTiZr	γ_s 100	–	–	1.767
	γ_s 110	–	–	1.531
	γ_{usf} 110	–	–	0.463
	γ_{usf} 112	–	–	0.526
MoNbTi	γ_s 100	2.317	–	2.087
	γ_s 110	2.171	–	1.804
	γ_{usf} 110	0.820	–	0.725
	γ_{usf} 112	0.927	–	0.812
MoNbTaVW	γ_s 100	3.012	3.477	2.479
	γ_s 110	2.645	2.909	2.053
	γ_{usf} 110	1.176	1.448	0.979
	γ_{usf} 112	1.215	1.447	1.115
MoNbTaW	γ_s 100	3.188	3.667	2.530
	γ_s 110	2.684	2.943	2.156
	γ_{usf} 110	1.286	1.584	1.034
	γ_{usf} 112	1.325	1.602	1.198

in the isotropic case, which is balanced by the critical energy for surface creation, i.e. $G = G_c = 2\gamma_s$. The mixed-mode critical stress intensity for cleavage, compared to the mode I-only stress intensity (K_{Ic}), is

$$\frac{K_{Ic}^{mix}}{K_{Ic}} = \left[1 + \left(\frac{K_{II}}{K_I} \right)^2 + \frac{1}{1-\nu} \left(\frac{K_{III}}{K_I} \right)^2 \right]^{-1/2} \quad (\text{A.2})$$

Using the constrained path approximation, Rice (1992) provides the isotropic formulation for emission on an inclined slip plane at $\theta > 0$ with the Burgers vector angled at ϕ with respect to the crack front normal. The mixed-mode critical stress intensity for emission, compared to the mode I-only stress intensity (K_{Ie}), is

$$\frac{K_{Ie}^{mix}}{K_{Ie}} = \left[1 \pm \frac{K_{II}}{K_I} \left(2 \csc \theta - 3 \tan \frac{\theta}{2} \right) \pm 2 \frac{K_{III}}{K_I} \csc \theta \tan \phi \right]^{-1} \quad (\text{A.3})$$

From Eq. (A.2), the decrease in the critical stress intensity for cleavage by mixed-mode loading scales $\sim 1/s^2$, where s is the amount of shear. In comparison, from Eq. (A.3), the scaling is $\sim 1/s$. Consequently, we generally expect mixed-mode loading to improve ductility, since the critical stress intensity for emission decreases faster than for cleavage. The mixed-mode ductility index, compared to the mode I-only index (D), is

$$\frac{D^{mix}}{D} = \frac{K_{Ie}^{mix}}{K_{Ie}} \left[\frac{K_{Ic}^{mix}}{K_{Ic}} \right]^{-1} = \frac{\sqrt{1 + \left(\frac{K_{II}}{K_I} \right)^2 + \frac{1}{1-\nu} \left(\frac{K_{III}}{K_I} \right)^2}}{1 \pm \frac{K_{II}}{K_I} \left(2 \csc \theta - 3 \tan \frac{\theta}{2} \right) \pm 2 \frac{K_{III}}{K_I} \csc \theta \tan \phi} \quad (\text{A.4})$$

which is illustrated in Fig. 7 for the crack orientations studied.

References

- Alers, G.A., 1960. Elastic moduli of vanadium. *Phys. Rev.* 119 (5), 1532–1535.
- Allard, S. (Ed.), 1969. III - Elastic constants. In: *Metals*. Pergamon, pp. 72–90.
- Andric, P., Curtin, W.A., 2017. New theory for Mode I crack-tip dislocation emission. *J. Mech. Phys. Solids* 106, 315–337.
- Andric, P., Curtin, W.A., 2019. Atomistic modeling of fracture. *Modelling Simulation Mater. Sci. Eng.* 27 (1), 013001.
- Andric, P., Yin, B., Curtin, W.A., 2019. Stress-dependence of generalized stacking fault energies. *J. Mech. Phys. Solids* 122, 262–279.
- Argon, A.S., 2008. *Strengthening mechanisms in crystal plasticity*. Oxford University Press.
- Ayres, R.A., Shannette, G.W., Stein, D.F., 1975. Elastic constants of tungsten–rhenium alloys from 77 to 298 °K. *J. Appl. Phys.* 46 (4), 1526–1530.
- Bergegeay, C., Bernard, S., 2005. First-principles equations of state and elastic properties of seven metals. *Phys. Rev. B* 72 (21), 214101.
- Bolef, D.I., 1961. Elastic constants of single crystals of the bcc transition elements V, Nb, and Ta. *J. Appl. Phys.* 32 (1), 100–105.
- Bolef, D.I., De Klerk, J., 1962. Elastic constants of single-crystal Mo and W between 77° and 500 °K. *J. Appl. Phys.* 33 (7), 2311–2314.
- Bolef, D.I., Smith, R.E., Miller, J.G., 1971. Elastic properties of vanadium. I. Temperature dependence of the elastic constants and the thermal expansion. *Phys. Rev. B* 3 (12), 4100–4108.
- Carroll, K.J., 1965. Elastic constants of niobium from 4.2° to 300 °K. *J. Appl. Phys.* 36 (11), 3689–3690.
- Chen, S., Yang, X., Dahmen, K., Liaw, P., Zhang, Y., 2014. Microstructures and crackling noise of AlxNbTiMoV high entropy alloys. *Entropy* 16 (2), 870–884.
- Coury, F.G., Kaufman, M., Clarke, A.J., 2019. Solid-solution strengthening in refractory high entropy alloys. *Acta Mater.* 175, 66–81.
- Curtin, W.A., 1990. On lattice trapping of cracks. *J. Mater. Res.* 5 (7), 1549–1560.
- Davidson, D.L., Brotzen, F.R., 1968. Elastic constants of Molybdenum-Rich Rhenium alloys in the temperature range –190 °C to +100 °C. *J. Appl. Phys.* 39 (12), 5768–5775.

- Dickinson, J.M., Armstrong, P.E., 1967. Temperature dependence of the elastic constants of molybdenum. *J. Appl. Phys.* 38 (2), 602–606.
- Featherston, F.H., Neighbours, J.R., 1963. Elastic constants of tantalum, tungsten, and molybdenum. *Phys. Rev.* 130 (4), 1324–1333.
- Fisher, E.S., Westlake, D.G., Ockers, S.T., 1975. Effects of hydrogen and oxygen on the elastic moduli of vanadium, niobium, and tantalum single crystals. *Phys. Status Solidi a* 28 (2), 591–602.
- Giannattasio, A., Roberts, S.G., 2007. Strain-rate dependence of the brittle-to-ductile transition temperature in tungsten. *Phil. Mag.* 87 (17), 2589–2598.
- Gordon, P.A., Neeraj, T., Luton, M.J., 2008. Atomistic simulation of dislocation nucleation barriers from cracktips in α -Fe. *Modelling Simulation Mater. Sci. Eng.* 16 (4), 045006.
- Gorsse, S., Miracle, D.B., Senkov, O.N., 2017. Mapping the world of complex concentrated alloys. *Acta Mater.* 135, 177–187.
- Griffith, A.A., Taylor, G.I., 1921. VI. The phenomena of rupture and flow in solids. *Proc. R. Soc. Lond. Ser. A Math. Phys. Eng. Sci.* 221 (582), 163–198.
- Gumbsch, P., 2003. Brittle fracture and the brittle-to-ductile transition of tungsten. *J. Nucl. Mater.* 323 (2), 304–312.
- Heiming, A., Petry, W., Trampenau, J., Alba, M., Herzig, C., Schober, H.R., Vogl, G., 1991. Phonon dispersion of the bcc phase of group-IV metals. II. bcc zirconium, a model case of dynamical precursors of martensitic transitions. *Phys. Rev. B* 43 (13), 10948–10962.
- Henkelman, G., Uberuaga, B.P., Jónsson, H., 2000. A climbing image nudged elastic band method for finding saddle points and minimum energy paths. *J. Chem. Phys.* 113 (22), 9901–9904.
- Hirsch, P.B., Roberts, S.G., 1991. The brittle-ductile transition in silicon. *Phil. Mag. A* 64 (1), 55–80.
- Hu, Y.-J., Sundar, A., Ogata, S., Qi, L., 2021. Screening of generalized stacking fault energies, surface energies and intrinsic ductile potency of refractory multicomponent alloys. *Acta Mater.* (in press).
- Ikehata, H., Nagasako, N., Furuta, T., Fukumoto, A., Miwa, K., Saito, T., 2004. First-principles calculations for development of low elastic modulus Ti alloys. *Phys. Rev. B* 70 (17), 174113.
- Joseph, T., Tanaka, M., Wilkinson, A., Roberts, S., 2007. Brittle–ductile transitions in vanadium and iron–chromium. *J. Nucl. Mater.* 367–370, 637–643.
- Katahara, K.W., Manghnani, M.H., Fisher, E.S., 1979. Pressure derivatives of the elastic moduli of BCC Ti-V-Cr, Nb-Mo and Ta-W alloys. *J. Phys. F* 9 (5), 773–790.
- Koči, L., Ma, Y., Oganov, A.R., Souvatzis, P., Ahuja, R., 2008. Elasticity of the superconducting metals V, Nb, Ta, Mo, and W at high pressure. *Phys. Rev. B* 77 (21), 214101.
- Kresse, G., Furthmüller, J., 1996. Efficient iterative schemes for *ab initio* total-energy calculations using a plane-wave basis set. *Phys. Rev. B* 54 (16), 11169–11186.
- Kresse, G., Joubert, D., 1999. From ultrasoft pseudopotentials to the projector augmented-wave method. *Phys. Rev. B* 59 (3), 1758–1775.
- Ledbetter, H., Ogi, H., Kai, S., Kim, S., Hirao, M., 2004. Elastic constants of body-centered-cubic titanium monocrystals. *J. Appl. Phys.* 95 (9), 4642–4644.
- Li, X., Li, W., Irving, D.L., Varga, L.K., Vitos, L., Schönecker, S., 2020. Ductile and brittle crack-tip response in equimolar refractory high-entropy alloys. *Acta Mater.* 189, 174–187.
- Liao, M., Liu, Y., Cui, P., Qu, N., Zhou, F., Yang, D., Han, T., Lai, Z., Zhu, J., 2020. Modeling of alloying effect on elastic properties in BCC Nb-Ti-V-Zr solid solution: From unary to quaternary. *Comput. Mater. Sci.* 172, 109289.
- Liaw, P., 2020. Private communication.
- Liu, Z., Shang, J., 2011. First principles calculations of electronic properties and mechanical properties of bcc molybdenum and niobium. *Rare Metals* 30 (1), 354–358.
- Lowrie, R., Gonas, A.M., 1967. Single-crystal elastic properties of tungsten from 24° to 1800 °C. *J. Appl. Phys.* 38 (11), 4505–4509.
- Magerl, A., Berre, B., Alefeld, G., 1976. Changes of the elastic constants of V, Nb, and Ta by hydrogen and deuterium. *Phys. Status Solidi a* 36 (1), 161–171.
- Mak, E., Curtin, W.A., 2020. Intrinsic fracture behavior of Mg–Y alloys. *Modelling Simulation Mater. Sci. Eng.* 28 (3), 035012.
- Maresca, F., Curtin, W.A., 2020a. Mechanistic origin of high strength in refractory BCC high entropy alloys up to 1900 K. *Acta Mater.* 182, 235–249.
- Maresca, F., Curtin, W.A., 2020b. Theory of screw dislocation strengthening in random BCC alloys from dilute to “High-Entropy” alloys. *Acta Mater.* 182, 144–162.
- Methfessel, M., Paxton, A.T., 1989. High-precision sampling for Brillouin-zone integration in metals. *Phys. Rev. B* 40 (6), 3616–3621.
- Miracle, D., Miller, J., Senkov, O., Woodward, C., Uchic, M., Tiley, J., Miracle, D.B., Miller, J.D., Senkov, O.N., Woodward, C., Uchic, M.D., Tiley, J., 2014. Exploration and development of high entropy alloys for structural applications. *Entropy* 16 (1), 494–525.
- Miracle, D.B., Senkov, O.N., 2017. A critical review of high entropy alloys and related concepts. *Acta Mater.* 122, 448–511.
- Möller, J.J., Bitzek, E., 2014. Comparative study of embedded atom potentials for atomistic simulations of fracture in α -iron. *Modelling Simulation Mater. Sci. Eng.* 22 (4), 045002.
- Monkhorst, H.J., Pack, J.D., 1976. Special points for Brillouin-zone integrations. *Phys. Rev. B* 13 (12), 5188–5192.
- Nagasako, N., Jahnátek, M., Asahi, R., Hafner, J., 2010. Anomalies in the response of V, Nb, and Ta to tensile and shear loading: *Ab initio* density functional theory calculations. *Phys. Rev. B* 81 (9), 094108.
- Northcott, L., 1961. Some features of the refractory metals. *J. Less Common Metals* 3 (2), 125–148.
- Ohr, S., 1985. An electron microscope study of crack tip deformation and its impact on the dislocation theory of fracture. *Mater. Sci. Eng.* 72 (1), 1–35.
- Perdew, J.P., Burke, K., Ernzerhof, M., 1996. Generalized gradient approximation made simple. *Phys. Rev. Lett.* 77 (18), 3865–3868.
- Plimpton, S., 1995. Fast parallel algorithms for short-range molecular dynamics. *J. Comput. Phys.* 117 (1), 1–19.
- Raffo, P., 1969. Yielding and fracture in tungsten and tungsten-rhenium alloys. *J. Less Common Metals* 17 (2), 133–149.
- Rao, S.I., Akdim, B., Antillon, E., Woodward, C., Parthasarathy, T.A., Senkov, O.N., 2019a. Modeling solution hardening in BCC refractory complex concentrated alloys: NbTiZr, Nb_{1.5}TiZr_{0.5} and Nb_{0.5}TiZr_{1.5}. *Acta Mater.* 168, 222–236.
- Rao, S.I., Woodward, C., Akdim, B., Antillon, E., Parthasarathy, T.A., Senkov, O.N., 2019b. Estimation of diffusional effects on solution hardening at high temperatures in single phase compositionally complex body centered cubic alloys. *Scr. Mater.* 172, 135–137.
- Rice, J.R., 1992. Dislocation nucleation from a crack tip: An analysis based on the Peierls concept. *J. Mech. Phys. Solids* 40 (2), 239–271.
- Roberts, S.G., Hirsch, P.B., Booth, A.S., Ellis, M., Serbena, F.C., 1993. Dislocations, cracks and brittleness in single crystals. *Phys. Scr. T49B*, 420–426.
- Senkov, O., Rao, S., Butler, T., Chaput, K., 2019. Ductile Nb alloys with reduced density and cost. *J. Alloys Compd.* 808, 151685.
- Senkov, O., Rao, S., Chaput, K., Woodward, C., 2018. Compositional effect on microstructure and properties of NbTiZr-based complex concentrated alloys. *Acta Mater.* 151, 201–215.
- Senkov, O.N., Scott, J.M., Senkova, S.V., Meisenkothen, F., Miracle, D.B., Woodward, C.F., 2012. Microstructure and elevated temperature properties of a refractory TaNbHfZrTi alloy. *J. Mater. Sci.* 47 (9), 4062–4074.
- Senkov, O., Scott, J., Senkova, S., Miracle, D., Woodward, C., 2011a. Microstructure and room temperature properties of a high-entropy TaNbHfZrTi alloy. *J. Alloys Compd.* 509 (20), 6043–6048.
- Senkov, O., Senkova, S., Woodward, C., 2014. Effect of aluminum on the microstructure and properties of two refractory high-entropy alloys. *Acta Mater.* 68, 214–228.
- Senkov, O.N., Wilks, G.B., Miracle, D.B., Chuang, C.P., Liaw, P.K., 2010. Refractory high-entropy alloys. *Intermetallics* 18 (9), 1758–1765.
- Senkov, O.N., Wilks, G.B., Scott, J.M., Miracle, D.B., 2011b. Mechanical properties of Nb₂₅Mo₂₅Ta₂₅W₂₅ and V₂₀Nb₂₀Mo₂₀Ta₂₀W₂₀ refractory high entropy alloys. *Intermetallics* 19 (5), 698–706.
- Shang, S., Saengdeejing, A., Mei, Z., Kim, D., Zhang, H., Ganeshan, S., Wang, Y., Liu, Z., 2010. First-principles calculations of pure elements: Equations of state and elastic stiffness constants. *Comput. Mater. Sci.* 48 (4), 813–826.
- Söderlind, P., Eriksson, O., Wills, J.M., Boring, A.M., 1993. Theory of elastic constants of cubic transition metals and alloys. *Phys. Rev. B* 48 (9), 5844–5851.

- Spitzig, W., Owen, C., 1987. Effect of the nitrogen-to-hydrogen ratio on the mechanical behavior of vanadium, niobium and tantalum. *Mater. Sci. Eng.* 91, 97–104.
- Stukowski, A., 2010. Visualization and analysis of atomistic simulation data with OVITO—the open visualization tool. *Modelling Simulation Mater. Sci. Eng.* 18 (1), 015012.
- Swinburne, T.D., Marinica, M.-C., 2018. Unsupervised calculation of free energy barriers in large crystalline systems. *Phys. Rev. Lett.* 120 (13).
- Thomson, R., Hsieh, C., Rana, V., 1971. Lattice trapping of fracture cracks. *J. Appl. Phys.* 42 (8), 3154–3160.
- Ting, T.T.C., 1996. Anisotropic elasticity: Theory and applications. In: Oxford Engineering Science Series, Oxford University Press, Oxford, New York.
- Tyson, W., Ayres, R., Stein, D., 1973. Anisotropy of cleavage in B.C.C. transition metals. *Acta Metall.* 21 (5), 621–627.
- Varvenne, C., Luque, A., Nöhling, W.G., Curtin, W.A., 2016. Average-atom interatomic potential for random alloys. *Phys. Rev. B* 93 (10), 104201.
- Walker, E., Peter, M., 1977. Elastic constants of the bcc phase in niobium–zirconium alloys between 4.2 and 300 K. *J. Appl. Phys.* 48 (7), 2820–2826.
- Yang, C., Qi, L., 2018. Ab initio calculations of ideal strength and lattice instability in W-Ta and W-Re alloys. *Phys. Rev. B* 97 (1), 014107.
- Yao, H., Qiao, J.-W., Gao, M., Hawk, J., Ma, S.-G., Zhou, H., 2016a. MoNbTaV medium-entropy alloy. *Entropy* 18 (5), 189.
- Yao, H., Qiao, J., Gao, M., Hawk, J., Ma, S., Zhou, H., Zhang, Y., 2016b. NbTaV-(Ti,W) refractory high-entropy alloys: Experiments and modeling. *Mater. Sci. Eng. A* 674, 203–211.
- Yin, B., Wu, Z., Curtin, W.A., 2017. Comprehensive first-principles study of stable stacking faults in hcp metals. *Acta Mater.* 123, 223–234.
- Zhou, X.W., Wadley, H.N.G., Johnson, R.A., Larson, D.J., Tabat, N., Cerezo, A., Petford-Long, A.K., Smith, G.D.W., Clifton, P.H., Martens, R.L., Kelly, T.F., 2001. Atomic scale structure of sputtered metal multilayers. *Acta Mater.* 49 (19), 4005–4015.
- Zhu, T., Li, J., Samanta, A., Kim, H.G., Suresh, S., 2007. Interfacial plasticity governs strain rate sensitivity and ductility in nanostructured metals. *Proc. Natl. Acad. Sci.* 104 (9), 3031–3036.
- Zunger, A., Wei, S.-H., Ferreira, L.G., Bernard, J.E., 1990. Special quasirandom structures. *Phys. Rev. Lett.* 65 (3), 353–356.